Connecticut College
Digital Commons @ Connecticut College

Chemistry Honors Papers | Chemistry Department

2014

Transition-Metal-Doped Manganese Oxide Hollow Nanospheres: Synthesis and Catalytic Activityc

Jeffrey Carmichael

Follow this and additional works at: http://digitalcommons.conncoll.edu/chemhp

Recommended Citation
Carmichael, Jeffrey, "Transition-Metal-Doped Manganese Oxide Hollow Nanospheres: Synthesis and Catalytic Activityc" (2014). *Chemistry Honors Papers*. Paper 12.
http://digitalcommons.conncoll.edu/chemhp/12

This Honors Paper is brought to you for free and open access by the Chemistry Department at Digital Commons @ Connecticut College. It has been accepted for inclusion in Chemistry Honors Papers by an authorized administrator of Digital Commons @ Connecticut College. For more information, please contact bpancier@conncoll.edu.
The views expressed in this paper are solely those of the author.

Transition-Metal-Doped Manganese Oxide Hollow Nanospheres: Synthesis and Catalytic Activity

Jeffrey Carmichael ‘14

Department of Chemistry, Connecticut College, New London, CT 06320

Advisor: Stanton Ching

Readers: Tanya Schneider and Steven Suib

Table of Contents

Acknowledgements

First of all, I must thank Professor Stanton “Stan” Ching for all he has done for me. From initially letting me join his lab my freshman year, to supporting my research for two summers and my sophomore and senior year. He always motivated me to do my absolute best work, partly due to his positive encouraging attitude, and partly due to not ever wanting to disappoint his perpetual smile. Stan always let me be on my own when I wanted, and was there for help when I needed it. I would not have gotten this far without him, not even close. I could not have asked for a better advisor.

Much of my gratitude goes out to the lab mates I began my research career with: Ian Richter and Kathryn Tutunjian. Without them, that first summer here would have been far less enjoyable and productive. They provided valuable feedback, were great sources of nerdy lab jokes to ease the stress of some of the longer days in lab, and helped me to become who I am in lab—and out of lab—today. I also want to thank my *current* lab mates: Ian Richter (still here!), Cameron Johnson and Lizzy Stone. Our lab dynamic made my final year here in lab truly my best one.

Of course, I can’t forget Professor Timo Ovaska for allowing me to work in his organic lab my junior year, along with Sami Ovaska, Aaron Feldman ’13, Evan Landstrom ’13 and Maia Taft ‘13. Although I didn’t stay there for my thesis, it gave me invaluable lab skills and techniques, expanded my appreciation of research, and made me into a more disciplined, dedicated researcher overall. And of course I have to thank Timo’s dog, Diego, for coming into lab and being a fluffy, cute distraction from everything for a few hours!

I want to thank Professor Tanya Schneider and Professor Steven Suib (UConn) for valuable feedback on my thesis. Also, to Tanya, thank you for broadening my academic horizons to include biochemistry, a branch of chemistry I never expected to enjoy as much as I did in your class.

My thanks go out to Evelyn Bamford, always being around to talk about anything and for helping out the entire department immensely. We could always count on her to have a fresh pot of coffee in the morning, and Dunkin' Donuts before each seminar! I also must thank Professor Maureen "Mo" Ronau for being an overall awesome person, always being open to gossip, random conversations, helping with tough orgo problems or giving life lessons when we needed them. Also there is Vicki Fontneau, without whom I would not have gotten the experience prepping the general chemistry labs, which really helped me hit the ground running in lab as far as techniques and important calculations go.

The rest of the chemistry department also gets my gratitude for teaching me, giving me a home and being my nerdy family through my four years here. They were there for me through the bad times, and there with me for the good. In this department, I grew from a hyperactive, immature freshman who kind-of-sorta liked chemistry, into a (still hyperactive) mature senior with a true passion for chemistry and knowledge. Also, a special shoutout to all my tutees for getting me to enjoy teaching as much as I do.

Finally, I want to thank the Keck Foundation and CELS for funding my summer research here, allowing me to do a large chunk of the work put into this thesis.

Abstract

Manganese oxide hollow spheres with approximate MnO_2 stoichiometry were synthesized by aqueous precipitation with a redox reaction between Mn(II) and MnO_4^- in the presence of butyric acid. The butyric acid acts as a structure-directing agent, reducing the average particle size of the materials, while also acting as a soft template for the spheres to form. This is possible because butyric acid forms a thermodynamically stable microemulsion in water, which is unable to be broken up in solution. Without incorporation of the carboxylic acids, the materials have a surface area of 133 m^2/g, while with the addition of butyric acid, the surface area is increased to 233 m^2/g. By powder X-ray diffraction, these materials are seen to be amorphous, having no long-range order in their structure.

Manganese oxide hollow spheres are able to be isomorphously doped with various transition metals, including iron, copper and vanadium. These metals were chosen due to their proximity to manganese on the periodic table, thus having similar size, weight and oxidation states to manganese. Also, they have all been reported to enhance the catalytic activity of manganese oxide materials.

The iron-doped manganese oxides exhibited a drastic increase in surface area, up to 434 m^2/g. Copper-doped spheres gave up to 350 m^2/g, and vanadium-doped spheres brought it to 331 m^2/g. The presence of any of the metals increases the surface area of the undoped hollow spheres by at least 100 m^2/g, the reason for which is still unknown. At low concentrations of the metal dopant, each systems also exhibits a core-shell structure. In the case of the iron-doped materials, as the iron level increases, the spheres become solid. In the copper- and vanadium-doped systems, the

core-shell structures disappear at higher dopant amount, reverting back to regular hollow spheres.

The catalytic activity of all of these materials was tested by using the common catalytic system of isopropanol oxidation. Being a relatively simple system to use, a lab-mate and I assisted in building an apparatus to test this and combined it with the use of a gas chromatograph to measure the amount of isopropanol that is converted to acetone. This was tested by heating the catalysts up to 200° and 250° C. The undoped hollow spheres showed strong catalytic activity of about 90% conversion of isopropanol to acetone, with the copper and iron dopants having little effect on that efficiency. The vanadium doped materials however lowered the catalytic efficiency to 50-70% conversion. The oxidation of carbon monoxide was also briefly tested, and the copper-doped materials gave 100% conversion at 25° C, while the other systems proved far less efficient. This gives promise to the copper-doped materials at lower temperatures in the isopropanol system.

Introduction

Manganese oxides are some of the most abundant minerals on earth, and can commonly be found in natural sediments, soils and ores. They are also prominent in formations such as desert rock varnish and marine manganese nodules.[1] Desert rock varnish is formed by many manganese-containing microbial organisms leaving manganese residue on desert rocks upon decomposition, leaving a thin film of manganese oxide (Figure 1A).[2] Marine manganese nodules are primarily manganese and iron oxides, which collect in large deposits deep in the ocean. The dissolved manganese and iron build up around a seed particle over the course of millions of years, in a fashion similar to the formation of a pearl in an oyster.[3]

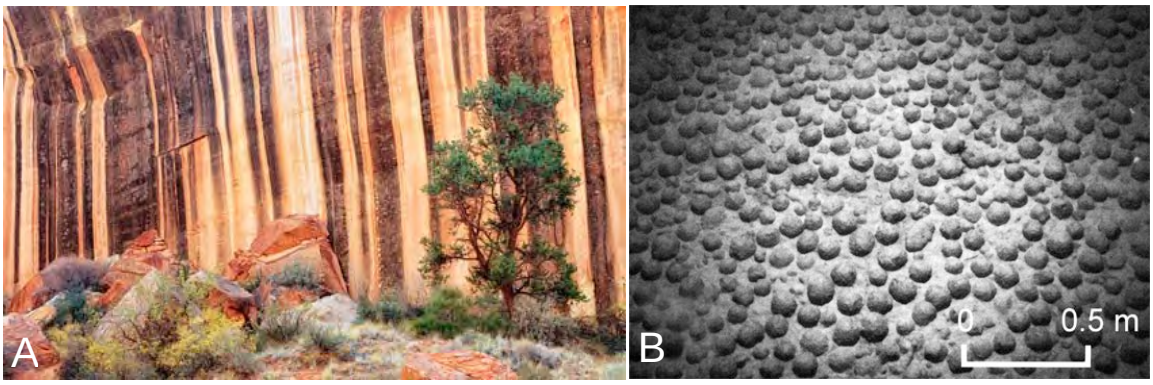

Photograph by: Larry Geddis (www.theguardian.com)

Photograph by: Ian Wright (Encyclopedia of New Zealand)

Figure 1. Manganese oxides in A) desert rock varnish and B) marine nodules

There are over 3 dozen naturally-occurring crystalline manganese oxide with approximate MnO_2 stoichiometry. In addition, there are many amorphous forms.[4,5] Crystalline architectures of these materials are comprised primarily of edge-shared MnO_6 octahedral units which are arranged to form tunneled or layered structures.

These structures contribute to the high porosity and surface areas of the manganese oxides. A few examples of crystalline tunneled and layered structures include the layered structure of birnessite and tunneled arrangements as seen in the 1x1 nonporous pyrolusite, 1x2 ramsdellite, 2x2 hollandite, 2x3 romanechite and 3x3 todorokite. Many of these materials have Mn(III)/Mn(IV) mixed-valency, imparting an overall negative charge to their framework. This allows the intercalation of cations and water molecules in tunnels or between layers, when there is an appropriately large volume. Due to high porosity, many manganese oxides exhibit high surface areas that are advantageous in potential applications related to rechargeable battery technology,[1,4,5] toxic waste remediation[1,6,7] and heterogeneous catalysis.[2,8-10]

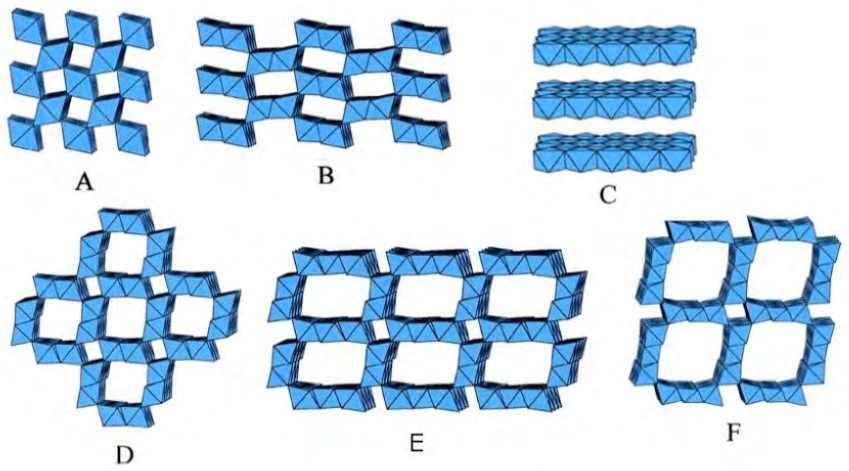

Figure 2. Crystalline structures of (A) pyrolusite, (B) ramsdellite, (C) birnessite, (D) hollandite, (E) romanechite, and (F) todorokite

Manganese oxides have a potential use in rechargeable batteries. Current Li-ion rechargeable batteries use graphite as the anode and a layered Li-CoO_2 similar to birnessite as the cathode (Figure 3). The high surface areas and facile ion exchange

capabilities of both Li-CoO_2 and graphite aid the mobility of and storage capacity for the Li^+ ions. Manganese oxides have attracted considerable interest as inexpensive (1/100th the cost) and non-toxic alternative materials as rechargeable battery cathodes.[1,4,5] However, an ongoing challenge is structural instability with repeated recharging cycles.

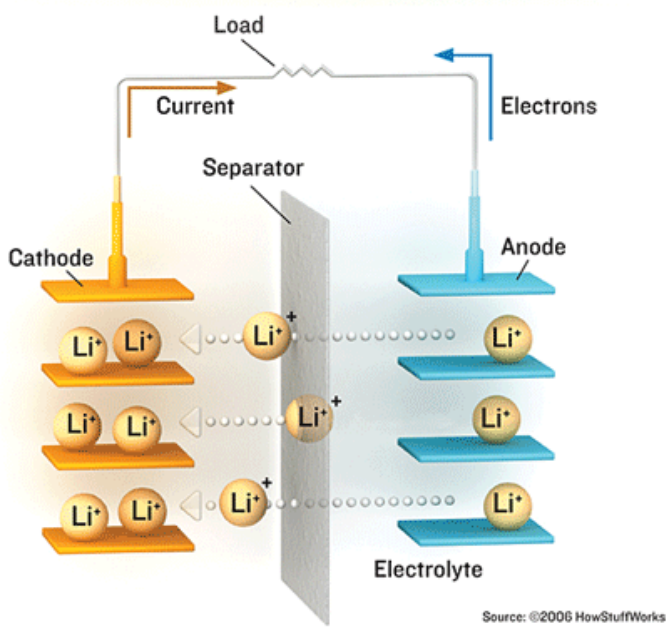

Figure 3. Lithium-ion rechargeable battery. Lithium ions travel between neutral graphite and negatively-charged CoO_2 material

In toxic waste remediation, Na-birnessite has been proposed as a material for removing heavy metal ions from an aqueous environment by ion-exchange. An example with Pb^{2+} is shown below in Figure 4. In this process, Pb^{2+} favorably exchanges with Na^+ from Na-birnessite and is incorporated into the layered framework, forming Pb-burserite. The concentrated lead ions can then be disposed of relatively easily.[1,6,7]

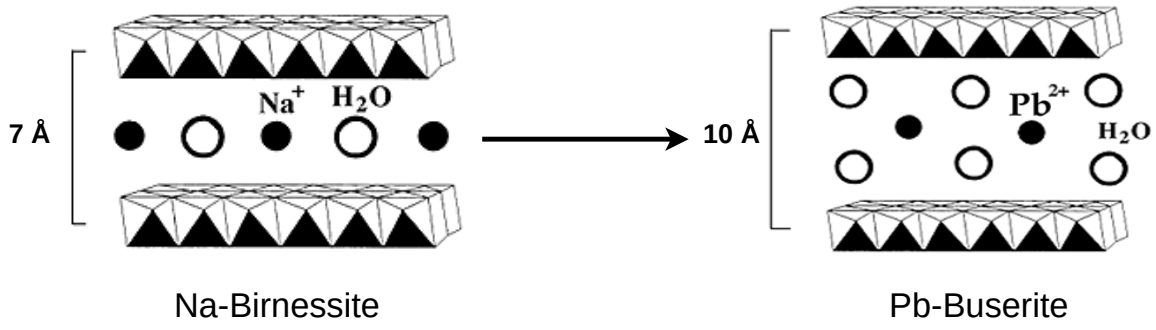

Figure 4. Reaction of Na-birnessite and Pb^{2+} to form Pb-burserite and Na^{+}.

Catalysis is an important process for many environmental and manufacturing applications.[11] Manganese oxides are particularly attractive because of their significantly lower cost than the noble metals, which are commonly used in many catalytic systems.[12] Manganese oxides are particularly well suited to perform oxidation reactions, and have shown considerable promise in processes such as the oxidation of carbon monoxide to carbon dioxide,[12-16] the conversion of alcohols into ketones, aldehydes or carboxylic acids,[9] the total oxidation of organics[8] and the reduction of oxygen.[17] Most of these reactions are thought to proceed by the Mars van Krevelen mechanism,[18] which is shown in Figure 5 for the oxidation of isopropanol to acetone. This mechanism highlights the versatility of manganese redox chemistry. Mn(IV) is reduced to Mn(II) as isopropanol is oxidized to acetone. Two hydrogen atoms on isopropanol are concomitantly transfered to a surface oxide to form water. The oxygen vacancy is then restored by reduction of O_2 and Mn(II) is reoxidized to Mn(IV). High-surface-area, nanostructured materials have been found to be particularly active catalysts in these types of oxidation reactions.[9,10] These materials are also of interest for their potential function in modern technologies like CO_2 lasers, pollution reduction

(catalytic converters) and the protection of Pt electrodes in hydrogen fuel cells which are readily deactivated by small concentrations of carbon monoxide.[13,14,17]

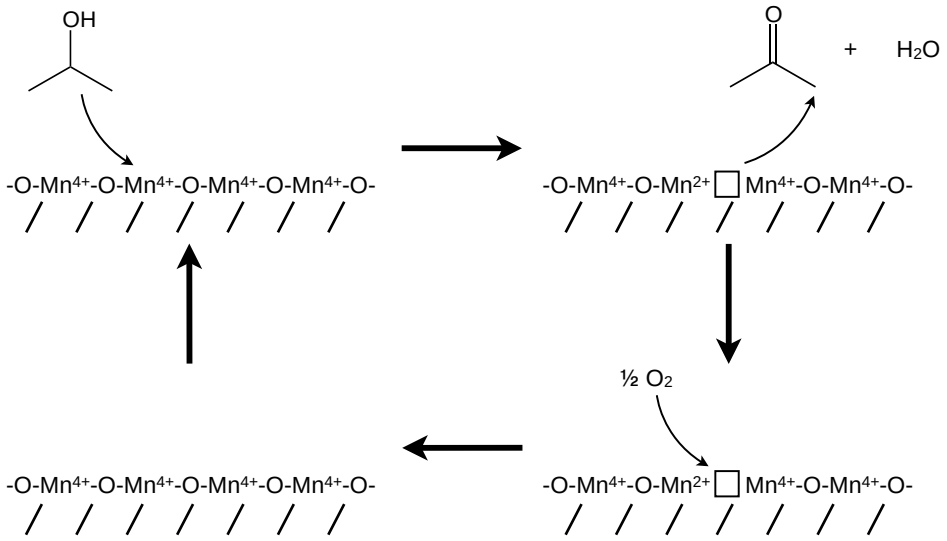

Figure 5. Mars van Krevelen mechanism applied to oxidation of isopropanol

A very desirable characteristic in all of these applications is high surface area. Surface area is important in rechargeable batteries because with a higher surface area, more Li^+ ions can be stored. In toxic waste remediation, more Pb^{2+} ions would be able to be removed with less material, and in heterogeneous catalysis, more interfacial contact increases the number of reactive sites, making the catalyst a more effective one. One prominent approach to improving the surface area of a material is increasing its porosity, which emphasizes the internal surface of a particle (Figure 6A). Another strategy is to decrease the particle size (Figure 6B).

A)

Steven Andrews (WM Earth Care)

B)

University of Walkato

Figure 6. Effect of A) porosity and B) particle size on surface area of a material

There are many synthetic routes to manganese oxides, including precipitation[19], ion-exchange[20], standard or microwave heating[21], high-temperature solid-state[22], hydrothermal[23] and sol-gel processes[24]. The conditions and methods of preparation can strongly influence the chemical and physical properties of these materials, even ones with seemingly identical composition and structure.[25] Various morphologies and subtle differences in the composition, average Mn oxidation state and surface structure can promote significantly different properties. As a result, the motivation to unearth novel synthetic approaches to manganese oxides continues to strengthen.

In the past decade, there has been considerable interest in designing nanostructured manganese oxides for applications that require high surface area and interfacial contact. Synthesized nanostructures have addressed both porosity and particle sIze while introducing a variety of morphologies that include textured spheres,

[26-28] nanorods and nanowires[19,26,27] and urchin-like spheres[17,19,29,30] (Figure 7). More complex forms have also been obtained, such as double-shell, core-shell and core-corona structures.[8,27,31,32] Many of these materials are synthesized with careful tailoring of the physical properties by using structure-directing agents such as templates and surfactants.[27,31] Hollow nanostructures are particularly interesting morphologies that can be synthesized by several methods, the most common of which are aged hydrothermal growth and the use of templates. In hydrothermal aging, the formation of the hollow nanospheres occurs in water at elevated temperature and pressure, and is often attributed to a process called Ostwald ripening.[33-36] Ostwald ripening involves an equilibrium between solid-liquid interfaces, where smaller, more soluble particles dissolve then redeposit as larger, more stable particles that typically have different morphology.[37,38] An example of Ostwald ripening is shown in Figure 8. Aggregated particles form by precipitation (Figure 8, 1h), then dissolve under hydrothermal conditions and diffuse to the outer surface of the aggregate. Here, they redeposit as larger particles with needle-like morphology, which creates a hollow urchin structure (8h). The redeposited particles tend to form in a spherical arrangement, which minimizes the surface energy. The dissolution of smaller particles from the core results in hollowing from the center.[33,37,38] This can also result in more complex hollow structures, such as core-shell structures, which contain a solid core within the hollow sphere (Figure 9).

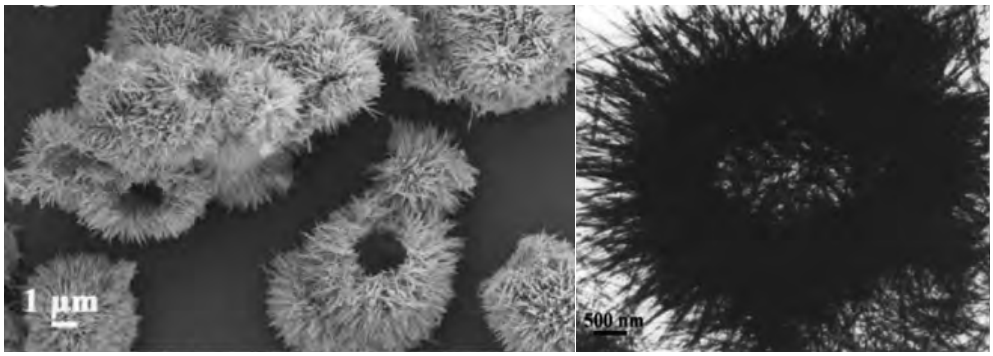

Figure 7. SEM (left) and TEM (right) of hollow, urchin-like nanoparticles.[17]

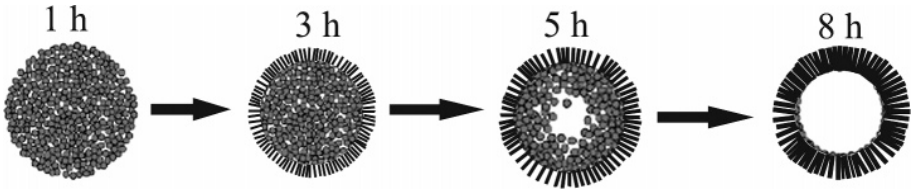

Figure 8. Process of Ostwald Ripening over a course of 8 hours.[37]

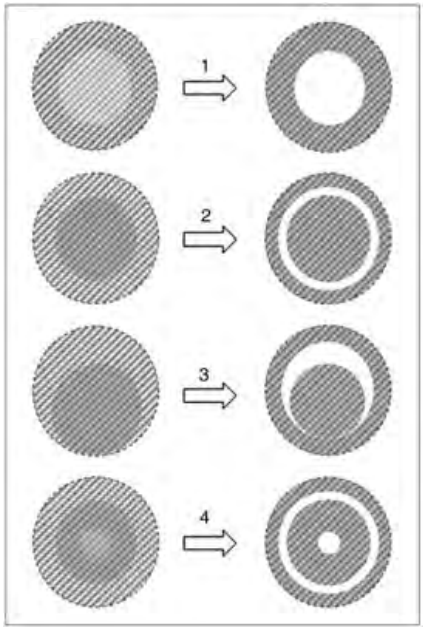

Figure 9. Diagram of Ostwald Ripening forming various higher-order nanospheres.[38]

Another hollow sphere synthetic process is called templating, and involves the use of a pre-formed structure around which a hollow sphere can be constructed. Templates are classified as being hard or soft, depending on the ease of their removal. An example of a hard-templating method is when spheres of known size—for instance SiO_2 or polymer beads—are added to the synthesis, and the MnO_2 particles accumulate on the surface. The spheres are subsequently etched away or burned off via calcination, leaving a hollow core behind (Figure 10).[34] The drawback of this approach is that this templating method is time consuming, and harsh chemical etching or calcining heat treatment can damage the MnO_2 shell.

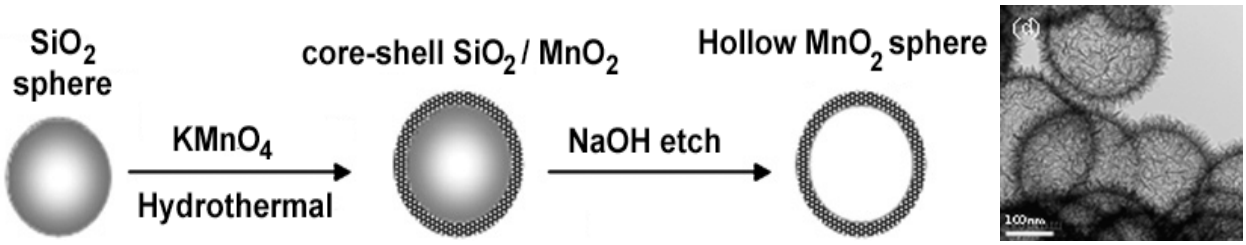

Figure 10. SiO_2 templating of hollow spheres[34]

Many of these manganese oxide materials mentioned can be synthesized from the redox reaction of MnO_4^- and Mn^{2+}. The reaction between MnO_4^- and Mn^{2+} is very commonly utilized in the area of nanoparticle synthesis because of the vast number of experimental parameters which are able to be varied. Previous research from the Ching research group established a facile, nearly instantaneous one-pot synthesis of monodisperse manganese oxide nanoparticles with this reaction, as well as the synthesis of hollow nanospheres in the presence of carboxylic acids.[39] In contrast, most

of the previously-described methods which can also be synthesized with this reaction require hydrothermal and other harsh conditions with reaction times ranging from hours to days.[17,34,37,38] Our synthesized materials are manganese oxide nanoparticles with approximate MnO_2 stoichiometry. These materials have hierarchical morphology[34], with different apparent structures depending on how closely they are inspected (Figure 11).[40] In the lower magnification SEM image (Figure 11A), the material appears to be made of solid, popcorn-shaped particles and not composed of any smaller particles. Once magnification is increased by TEM, however, the material appears to have a crumpled-tissue-paper morphology which is made up of minuscule sheets (Figure 11B). These materials are synthesized by a facile self-assembly route, in which the manganese oxides form on their own nearly instantly.[11] They have a surface area of 133 m^2/g.

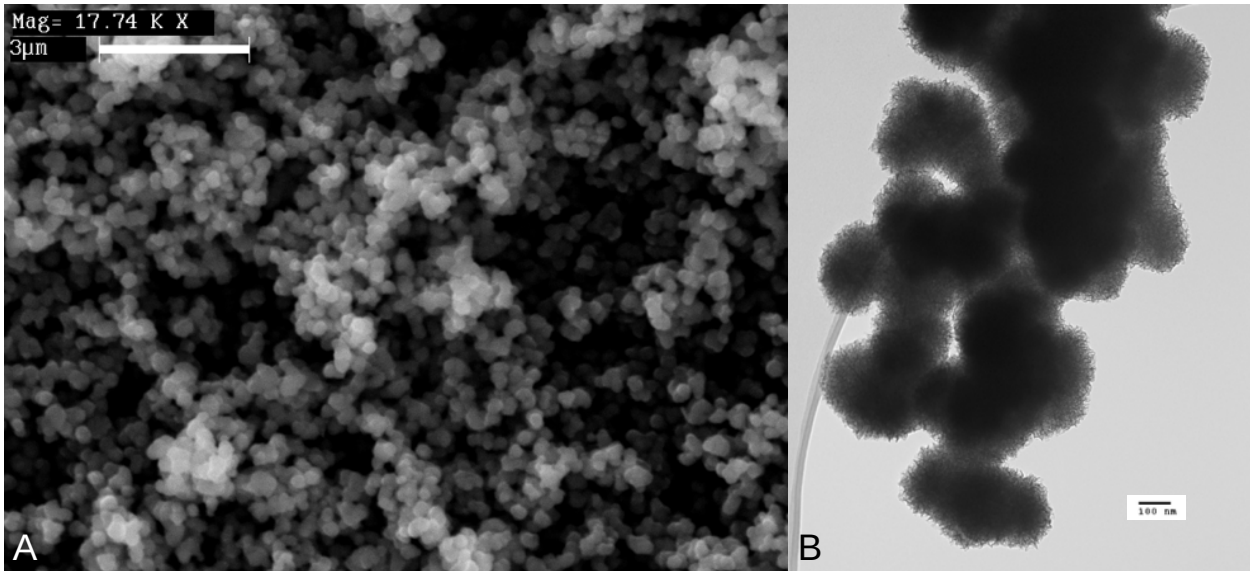

Figure 11. A) Low-mag SEM image of MnO_x nanoparticles, B) High-mag TEM image of MnO_x nanoparticles.[40]

To increase the surface area of these materials, this reaction is done in the presence of carboxylic acids. The inspiration for the use of carboxylic acids comes from their ability to stabilize the formation of Mn-12 clusters with the formula $Mn_{12}O_{12}(O_2CMe)_{16}(H_2O)_4$ when used in high concentrations (Figure 12).[41] In this system, carboxylate ligands (black) stabilize the formation of this Mn-12 cluster containing octahedral Mn centers (yellow), formed by a redox reaction between Mn^{2+} and MnO_4^-. In our approach, dilute carboxylic acids are used as structure-directing agents to arrest the growth to promote the formation of small particle sized, high surface area *materials*, though not so concentrated that individual *molecules* are formed. The carboxylic acid ligands being used instead of carboxylate ligands also aids in the formation of the materials rather than molecules, since carboxylate ligands coordinate more strongly than carboxylic acids.

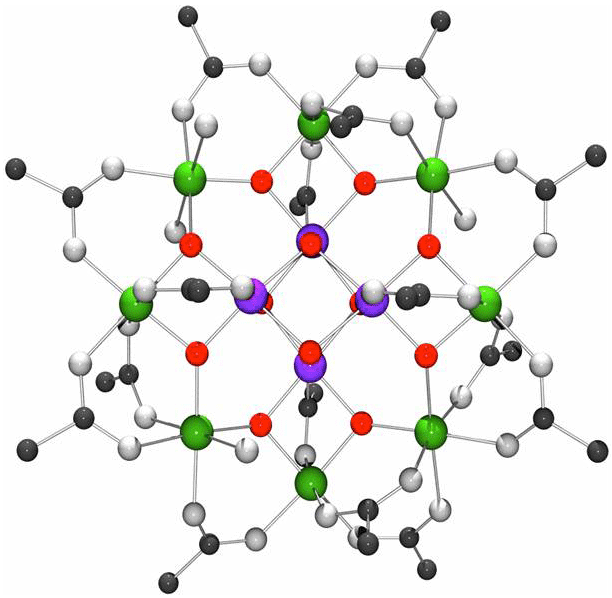

$$Mn(OAc)_2 + KMnO_4 \longrightarrow Mn_{12}O_{12}(O_2CCH_3)_{16}(H_2O)_4$$

Figure 12. Manganese-12 cluster molecule stabilized by carboxylate ligands (black)[41]

Various short-chain, water-miscible carboxylic acids were used, with butyric acid yielding the most interesting structures. When butyric acid is added, the materials adopt a spherical morphology. In lower magnification SEM images, the spheres appear to be solid MnO_x spheres, however under higher magnification TEM, the spheres appear to be hollow and are made up of very small platelets (Figure 13). These materials have a higher surface area (233 m^2/g) than the un-treated materials.[40]

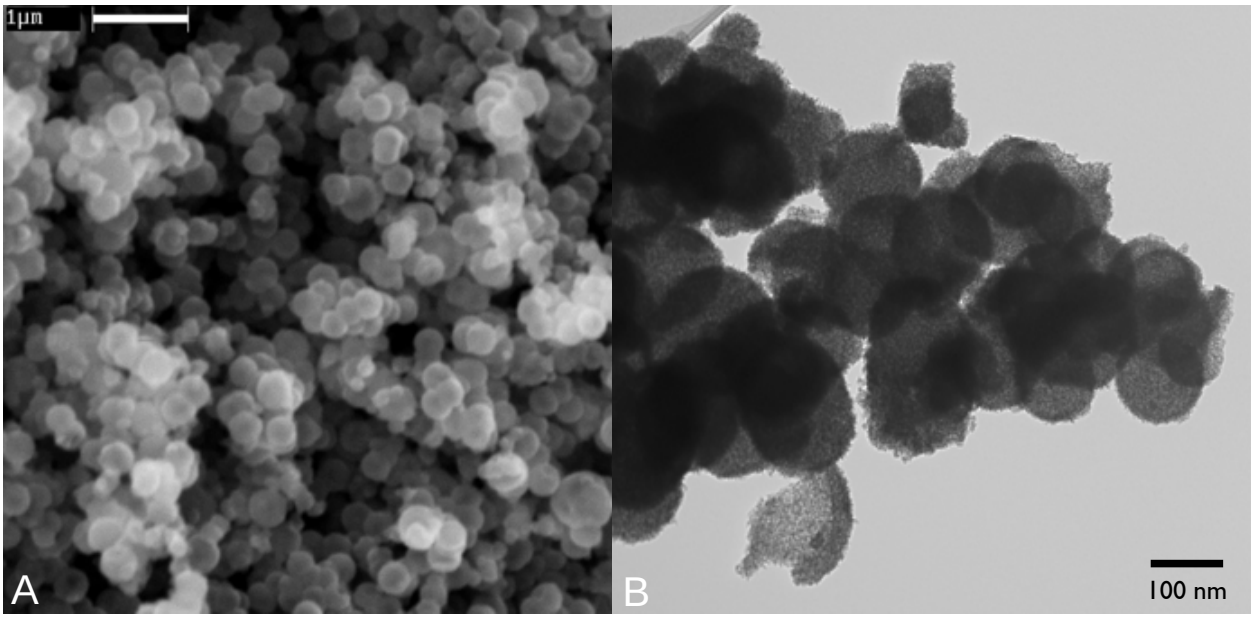

Figure 13. Hollow MnO_x nanospheres from the reaction of MnO_4^- and Mn^{2+} in the presence of butyric acid. A) SEM image (scale bar 1 µm), B) TEM image (note broken sphere on bottom, portrays hollowness)[40]

These spheres are thought to form by what is known as a soft templating method. In the proposed formation mechanism, butyric acid forms a microemulsion in the water, which is determined by the presence of the Tyndall effect tested with a green laser (Figure 14). The butyric acid (BA) emulsion acts as the template for the formation of the MnO_x hollow spheres under ambient conditions (Figure 15). In this mechanism,

the Mn^{2+} in the solution surrounding the BA emulsions reacts with MnO_4^- at the H_2O-BA interface while BA also functions as the structure-directing agent. Once the reaction is complete, the BA can easily be washed away with water, leaving the manganese oxide hollow spheres behind.

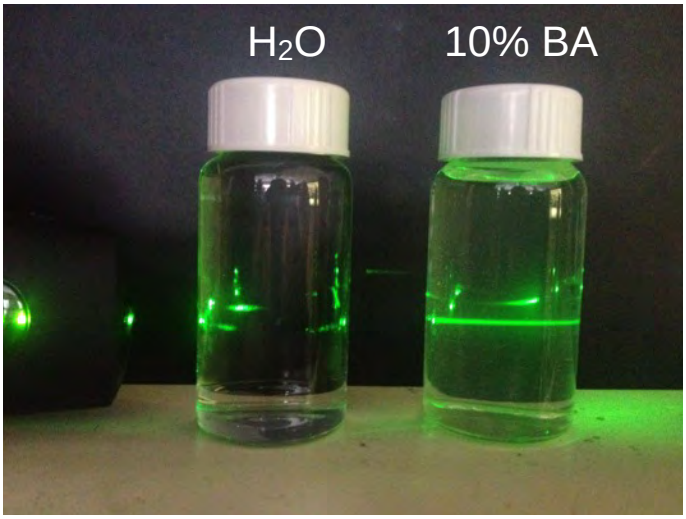

Figure 14. Tyndall effect demonstrated in solution of 2.3 mL butyric acid in ~25 mL H_2O with a green laser (from left)

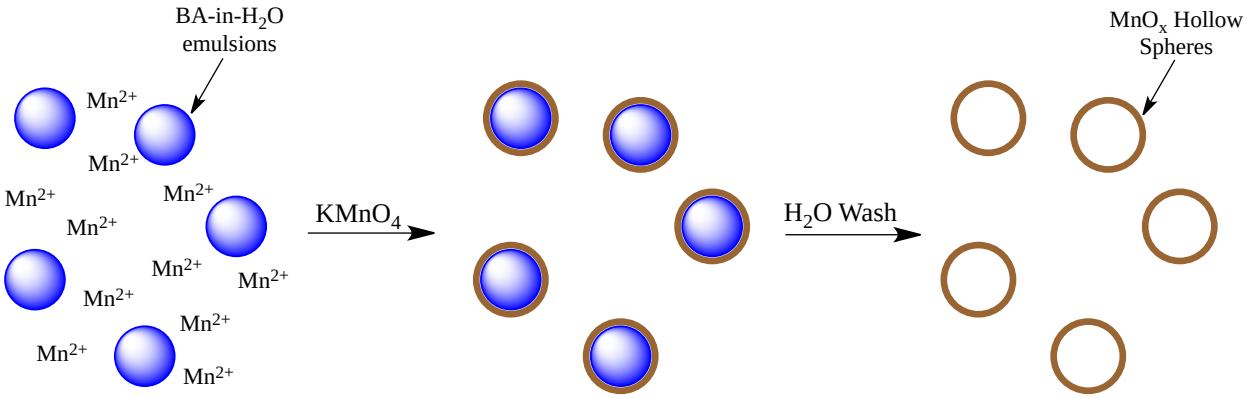

Figure 15. Proposed mechanism of hollow sphere formation with butyric acid micro-emulsion as soft template

The primary focus of this research is to investigate the influence of transition metal dopants on these hollow spheres and their catalytic activity in the oxidation of isopropanol. Our manganese oxide hollow spheres are able to be doped isomorphously with a number of transition metals.[42] The incorporation of these dopants can alter the chemical, physical, electrochemical and catalytic properties of the manganese oxides while having little effect on the nanostructure.[43] These dopants have been shown to affect the size, morphology and surface area of the materials.[10] The metals used in this study have been limited to Fe^{2+}, Cu^{2+} and V^{5+}. Fe and V were used due to their similar size and oxidation state to Mn, so that they would be able to efficiently replace Mn ions in the materials without disrupting the structure significantly. Cu was used due to its ability to improve catalytic activity in many other materials, while still being comparable to Mn on the periodic table.[15,44,45] Other common transition metal ions used are those which have similar charge, size and polarizability to Mn^{2+}, such as Co^{2+} and Zn^{2+}, while other metals such as Ce have been used as well.[43] The effects of transition-metal dopants on the manganese oxides in the realm of low-temperature oxidation have been explored more recently, especially with Cu-doped manganese oxides.[15,44,45] In our work with catalysis, one of my specific contributions was helping in setting up the custom flow reactor used to measure the catalytic activity of the materials in isopropanol oxidation.

Experimental

Syntheses of manganese oxide nanoparticles using carboxylic acids.

Manganese oxide nanoparticles were synthesized in the presence of carboxylic acids using the following general procedure: $KMnO_4$ (0.158 g, 1.0 mmol) and $MnSO_4 \bullet H_2O$ (0.254 g, 1.5 mmol) were each dissolved separately in 25 mL distilled H_2O. Carboxylic acids were then added in a 10-fold excess (versus total Mn) to the $MnSO_4$ solution. Carboxylic acids used were acetic acid (AA, 1.5 mL, 0.0175 mol/mL), propionic acid (PA, 1.9 mL, 0.0134 mol/mL) and butyric acid (BA, 2.3 mL, 0.0109 mol/mL). $KMnO_4$ solution was swiftly added to $MnSO_4$ solution with vigorous stirring. The resulting brown slurry was stirred vigorously for 20 minutes and vacuum-filtered through a glass frit. Brown solid was washed three times with H_2O and dried at 110° C. Typical yield is 0.22 g.

Fe^{2+}-doping with butyric acid present.

Reaction equations, stoichiometry quantities used in the $FeCl_2 \bullet 4H_2O$ reactions, and quantities used in the $Fe(NH_4)_2(SO_4)_2 \bullet 6H_2O$ reactions are given in Tables 1, 2 and 3, respectively. The amounts of $Fe(NH_4)_2(SO_4)_2 \bullet 6H_2O$, $MnSO_4 \bullet H_2O$ and BA used are summarized in Table 3.

Table 1: Redox equations of varying amounts of Fe^{2+} reacted with Mn^{2+} and MnO_4^-

Fe:Mn Ratio	Reaction Equation
0.051	$23\ Mn^{2+} + 2\ Fe^{2+} + 16\ MnO_4^- + 17\ H_2O \longrightarrow Fe_2Mn_{39}O_{81} + 34\ H^+$
0.083	$14\ Mn^{2+} + 2\ Fe^{2+} + 10\ MnO_4^- + 11\ H_2O \longrightarrow Fe_2Mn_{24}O_{51} + 22\ H^+$
0.11	$11\ Mn^{2+} + 2\ Fe^{2+} + 8\ MnO_4^- + 9\ H_2O \longrightarrow Fe_2Mn_{19}O_{41} + 18\ H^+$
0.22	$5\ Mn^{2+} + 2\ Fe^{2+} + 4\ MnO_4^- + 5\ H_2O \longrightarrow Fe_2Mn_9O_{21} + 10\ H^+$
0.35	$9\ Mn^{2+} + 6\ Fe^{2+} + 8\ MnO_4^- + 11\ H_2O \longrightarrow Fe_6Mn_4O_{11} + 6\ H^+$
0.5	$2\ Mn^{2+} + 2\ Fe^{2+} + 2\ MnO_4^- + 3\ H_2O \longrightarrow Fe_2Mn_4O_{11} + 6\ H^+$
1.0	$4\ Mn^{2+} + 10\ Fe^{2+} + 6\ MnO_4^- + 11\ H_2O \longrightarrow Fe_{10}Mn_{10}O_{35} + 22\ H^+$

Table 2: Amounts of $FeCl_2 \cdot 4H_2O$, $MnSO_4 \cdot H_2O$ and BA used

Fe:Mn Added	Mass of $FeCl_2 \cdot 4H_2O$	Mass of $MnSO_4 \cdot H_2O$	Volume of BA
0.051	0. 248 g	0.243 g	2.35 mL
0.11	0.0497 g	0.232 g	2.40 mL
0.22	0.0994 g	0.211 g	2.52 mL
0.35	0.149 g	0.190 g	2.63 mL

Table 3: Amounts of $Fe(NH_4)_2(SO_4)_2 \cdot 6H_2O$ and $MnSO_4 \cdot H_2O$ used

Fe:Mn Added	Mass of $Fe(NH_4)_2(SO_4)_2 \cdot 6H_2O$	Mass of $MnSO_4 \cdot H_2O$	Volume of BA
0.051	0.049 g	0.243 g	2.35 mL
0.083	0.078 g	0.237 g	2.39 mL
0.11	0.098 g	0.232 g	2.40 mL
0.22	0.196 g	0.211 g	2.52 mL
0.35	0.294 g	0.190 g	2.63 mL
0.5	0.392 g	0.169 g	2.75 mL
1.0	0.653 g	0.113 g	3.10 mL

Syntheses were also performed with $Fe(NH_4)_2(SO_4)_2 \cdot 6H_2O$ added in 0.1:1 to 0.6:1 ratios of Fe:Mn without regard to exact redox reaction stoichiometry. Six samples of 0.158 g $KMnO_4$ and 0.254 g $MnSO_4 \cdot H_2O$ were dissolved in 25 mL H_2O. $Fe(NH_4)_2(SO_4)_2 \cdot 6H_2O$ and BA were added to $MnSO_4$ solutions (Table 4). The Mn^{2+}/Fe^{2+} and $KMnO_4$ solutions were combined and stirred for 20 minutes. The resulting brown solid product was filtered through a medium-porosity glass frits, washed with H_2O and dried at 110° C.

Table 4: Amounts of $Fe(NH_4)_2(SO_4)_2 \cdot 6H_2O$ and BA used in non-stoichiometric synthesis

Fe:Mn Added	Mass of $Fe(NH_4)_2(SO_4)_2 \cdot 6H_2O$	Volume of BA
0.1	0.098 g	2.50 mL
0.2	0.196 g	2.75 mL
0.3	0.294 g	3.00 mL
0.4	0.392 g	3.20 mL
0.5	0.490 g	3.40 mL
0.6	0.588 g	3.70 mL

Fe^{2+}-doping with acetic acid, propionic acid and no acid present. Six samples of 0.158 g $KMnO_4$ were dissolved in 25 mL H_2O. $MnSO_4 \cdot H_2O$ and $Fe(NH_4)_2(SO_4)_2 \cdot 6H_2O$ were dissolved in 25 mL H_2O with acetic acid (AA) and propionic acid (PA) (Table 5). Solutions were combined and stirred for 20 minutes. For the acidic solutions only, dilution with 50 mL of distilled water was required to ease filtration. The brown solid products were filtered through medium-porosity glass frits, washed with H_2O and dried at 110° C.

Table 5: Amounts of $Fe(NH_4)_2(SO_4)_2•6H_2O$, $MnSO_4•H_2O$ and acid used

Fe:Mn Added	Mass of $Fe(NH_4)_2(SO_4)_2·6H_2O$	Mass of $MnSO_4·H_2O$	Volume of Acid
0.051	0.049 g	0.243 g	1.5 mL AA
0.051	0.049 g	0.243 g	1.9 mL PA
0.051	0.049 g	0.243 g	None
0.083	0.098 g	0.237 g	1.5 mL AA
0.083	0.098 g	0.237 g	2.0 mL PA
0.083	0.098 g	0.237 g	None

Cu^{2+}-doped MnO_x's. Five samples of $KMnO_4$ (0.158 g) and $MnSO_4•H_2O$ were dissolved separately in 25 mL H_2O. Varying amounts of $Cu(OAc)_2•H_2O$ and BA were added to the $MnSO_4•H_2O$ solutions (Table 6). The two solutions were combined and stirred for 20 minutes. The resulting brown solid was filtered through medium-porosity glass frits, washed with H_2O and dried at 110° C.

Table 6: Amounts of $Cu(OAc)_2•H_2O$ and BA used

Cu:Mn Added	Mass of $Cu(OAc)_2·H_2O$	Volume of BA
0.05	0.0250 g	2.4 mL
0.1	0.0499 g	2.5 mL
0.2	0.0998 g	2.75 mL
0.5	0.250 g	3.4 mL
1.0	0.499 g	4.6 mL

Cu^{2+}-doping with acetic acid, propionic acid and no acid present. Six samples of 0.158 g $KMnO_4$ and 0.254 g $MnSO_4 \cdot H_2O$ were dissolved separately in 25 mL H_2O. $Cu(OAc)_2 \cdot H_2O$ was added to $MnSO_4$ solutions with AA, PA or no acid (Table 7). Solutions were combined and stirred for 20 minutes. For the acidic solutions only, dilution with 50 mL of distilled water was required to ease filtration. The brown solid products were filtered through medium-porosity glass frits, washed with H_2O and dried at 110° C.

Table 7: Amounts of $Cu(OAc)_2 \cdot H_2O$ and acid used

Cu:Mn Added	Mass of $Cu(OAc)_2 \cdot H_2O$	Volume of Acid
0.2	0.0998 g	1.7 mL AA
0.2	0.0998 g	2.2 mL PA
0.2	0.0998 g	None
0.5	0.250 g	2.1 mL AA
0.5	0.250 g	2.8 mL PA
0.5	0.250 g	None

Cu^{2+}- and Fe^{2+}- doubly-doped MnO_x's. Six samples $KMnO_4$ (0.158 g) were dissolved in 25 mL H_2O. $Fe(NH_4)_2(SO_4)_2 \cdot 6H_2O$, $Cu(OAc)_2 \cdot H_2O$ and BA were added to solution of 0.254 g $MnSO_4 \cdot H_2O$ (Table 8). Solutions were combined, stirred for 20 minutes, and the resulting brown products were filtered, washed with H_2O then dried at 110° C.

Table 8: Amounts of $Fe(NH_4)_2(SO_4)_2 \cdot 6H_2O$, $Cu(OAc)_2 \cdot H_2O$ and BA used

Fe:Mn Added	Cu:Mn Added	Mass of $Fe(NH_4)_2(SO_4)_2 \cdot 6H_2O$	Mass of $Cu(OAc)_2 \cdot H_2O$	Volume of BA
0.051	**0.3**	0.049 g	0.150 g	2.4 mL
0.051	**1**	0.049 g	0.499 g	2.5 mL
0.11	**1**	0.098 g	0.499 g	2.6 mL
0.22	**1**	0.196 g	0.499 g	2.7 mL
0.22	**0.5**	0.196 g	0.250 g	2.6 mL
0.22	**0.3**	0.196 g	0.150 g	2.5 mL

Vanadium-doped MnO_x's. Five samples of $KMnO_4$ (0.158 g) and $MnSO_4 \cdot H_2O$ (0.254 g) were dissolved in 25 mL H_2O. Na_3VO_4 and BA were added to $MnSO_4$ solutions (Table 9), which turned opaque orange initially and became clear orange when BA was added. Solutions were combined, stirred for 20 minutes. The solid products were filtered through medium-porosity glass frits, washed with H_2O and dried at 110° C.

Table 9: Amounts of Na_3VO_4 and BA used

V:Mn Added	Mass of Na_3VO_4	Volume of BA
0.025	0.0115 g	2.4 mL
0.05	0.0233 g	2.4 mL
0.1	0.0460 g	2.5 mL
0.2	0.0920 g	2.8 mL
0.3	0.140 g	3.0 mL

Characterization Methods. Scanning electron microscopy (SEM) and energy dispersive X-ray analyses (EDAX) were carried out using a LEO 435VP Scanning Electron Microscope, Transmission electron microscopy (TEM) images were obtained using a Morgagni Instruments Transmission Electron Microscope. Elemental analyses were done with a Varian AA240FS Flame Atomic Absorption Spectrometer.

Thermogravimetric analyses (TGA) were performed using a TA Instruments model Q50 analyzer. Surface area analyses were measured using Brunauer-Emmett-Teller (BET) method of N_2 adsorption-desorption using a Micromeritics Gemini V Surface Area Analyzer. Samples were prepared for BET analysis by purging with N_2 at 200° C using a Micromeritics Flowprep 060 Sample Degas System. Powder X-ray diffraction was performed using a Rigaku Miniflex diffractometer.

Isopropanol Catalysis. A schematic for the catalytic reactions is shown in Figure 16. In a typical catalysis run, 0.10 g MnO_x was placed in glass tube held by glass wool plugs. The sample was heated in a tube furnace and purged at the prescribed temperature for one hour under a flow of 1% O_2 in He (40 mL/min). The gas was directed to bubble through the isopropanol reservoir. After 15 minutes, the resulting isopropanol/acetone mixture was collected in a glass tube cooled by liquid N_2 for 10 minutes. The frozen effluent was then thawed and analyzed by gas chromatography using a packed Carbowax column with TCD detection.

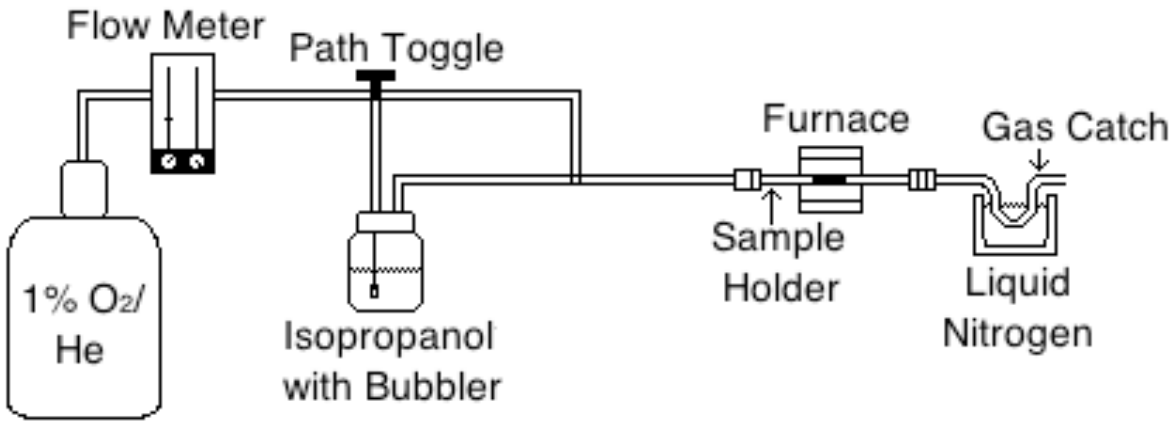

Figure 16. Schematic of catalysis setup for conversion of isopropanol to acetone

Carbon Monoxide Oxidation. The catalytic activity of MnO_x materials in CO oxidation was investigated using a fixed-bed gas flow reactor (Figure 17). For a typical run, 0.10 g MnO_x was placed into a U-shaped quartz tube held in with glass wool. Sample was heated to 200° C under He flow for 30 minutes. Gas flow was changed to 1% CO + 1% O_2 in N_2. Sample was allowed to equilibrate with reaction mixture for 20 minutes, then the flow was redirected to an online SRI 8610C gas chromatohraph equipped with a silica gel column and TCD detector.[39]

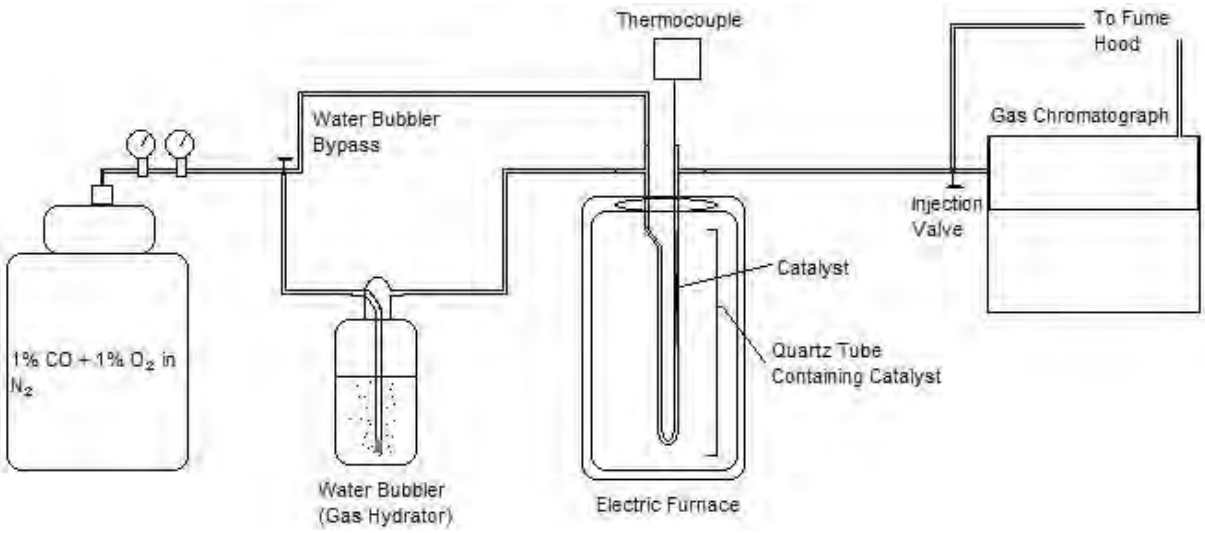

Figure 17. Schematic of flow reactor used for CO –> CO_2 catalysis measurements[39]

Results and Discussion

General Discussion

Manganese oxide nanoparticles have been synthesized by an aqueous redox reaction between MnO_4^- and Mn^{2+} (Equation 1), which is a common tactic in manganese oxide syntheses.[15,26,29,42,52,53] Previous group member David Kriz discovered that carboxylic acids act as interesting structure-directing agents in the synthesis of manganese oxide nanoparticles.[39] The inspiration for carboxylic acids being used in the reactions in the following pages comes from their ability to stabilize the formation of manganese oxide molecular clusters with the formula $Mn_{12}O_{12}(O_2CCH_3)_{16}(H_2O)_4$ (Figure 12) in high concentrations of the acids.[41] The high concentrations of carboxylic acids/carboxylate ligands drive the formation of the molecular cluster. From this, it was suggested that in dilute carboxylic acids, the coordination between the —COOH group and the nucleating MnO_x particles would minimize particle size and therefore increase surface area.[40] Acid added in a 10-fold excess to total metal was found to give the optimal hierarchical morphologies to the nanoparticles. Significantly higher concentrations of carboxylic acids caused the precipitate to be an oily solid, while lower concentrations caused the spheres to be less monodisperse.[39] The materials synthesized in this paper are made primarily by the use of butyric acid and other short-chain carboxylic acids.

$$2\,MnO_4^-\,(aq) + 3\,Mn^{2+}\,(aq) + 2\,H_2O\,(l) \longrightarrow 5\,MnO_2\,(s) + 4\,H^+\,(aq) \qquad (1)$$

When no carboxylic acid was used as a control (MnO_x-C) , the material assumed a “crumpled-tissue-paper” morphology made up of small platelets (Figure 18A).[27,40,46,47]

Materials made in the presence of acetic acid (MnO_x-AA) and propionic acid (MnO_x-PA) both exhibit a quasi-spherical morphology on the order of around 100 nm (Figure 18B+ 18C). In the presence of butyric acid, however, the material (MnO_x-BA) has adopted a hollow-spherical structure (Figure 18D).[40] SEM images of these materials are shown in Figure 19. The hollow spheres range in diameter from 200-400 nm, with their shells consisting of platelets on the order of 5-8 nm. The MnO_x-BA spheres are proven to be hollow by the existence of some broken shell fragments visible under TEM (Figure 13B).

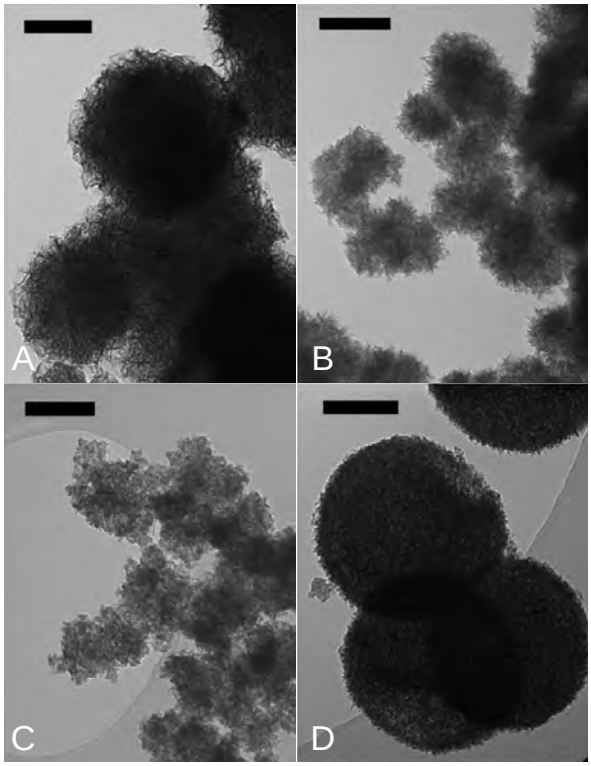

Figure 18. TEM images of MnO_x synthesized with A) no acid, B) acetic acid, C) propionic acid and D) butyric acid. Scale bar = 100 nm

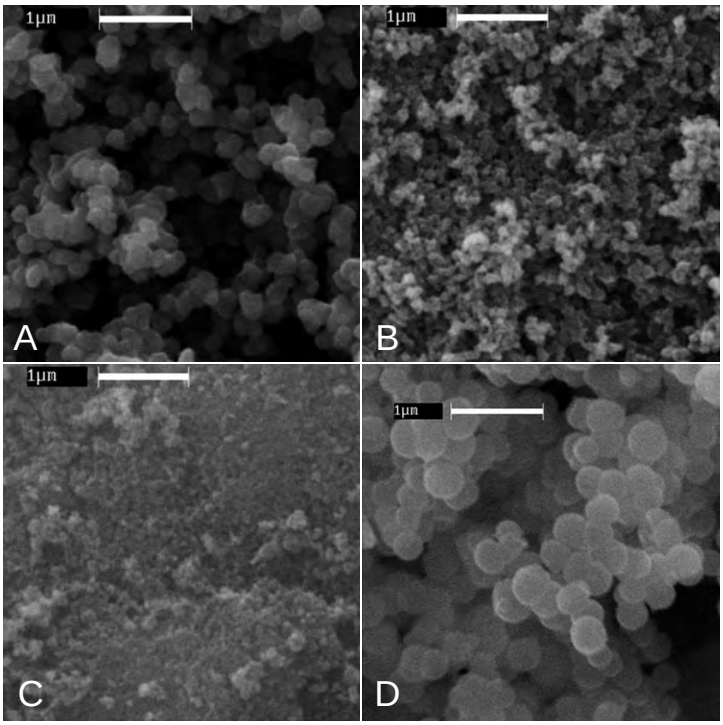

Figure 19. SEM images of MnO_x synthesized with A) no acid, B) acetic acid, C) propionic acid and D) butyric acid. Scale bar = 1 µm

Many other instances of hollow sphere formation have been reported,[10,33-36,47-51] but the significance of our spheres is their ease of formation. Most other syntheses involve hydrothermal conditions over the range of several hours or days, or involve complex templating methods which require several steps, as with the hard templating method shown in Figure 10.[10,33-38,50,51] Our hollow spheres form by a near-instant, self-assembly route under ambient conditions. Due to the interesting morphology of MnO_x-BA, this will be the focus of this study.

Elemental analysis, Mn oxidation state analysis and thermogravimetric analysis (TGA) indicate that each material has a similar composition, involving less than one water of hydration and trace amounts of potassium. FT-IR measurements indicate no presence of carboxylic acids remaining, further supporting our proposed formation

mechanism (Figure 15). BET measurements show that the carboxylic acids have a strong effect on the surface area of the materials, each having more than doubled the surface area of the control (Table 10).[40] The average oxidation state of Mn being less than 4 for all of the materials indicates that these materials are mixed-valent, containing both Mn(III) and Mn(IV).

Table 10: Analytical information on control and acid-treated MnO_x

MnO_x	Formula	Mn ox. state	Surface Area (m^2/g)
MnO_x-C	$K_{0.023}MnO_{1.91}\cdot 0.63H_2O$	3.88	133
MnO_x-AA	$K_{0.053}MnO_{2.01}\cdot 0.48H_2O$	3.86	307
MnO_x-PA	$K_{0.042}MnO_{1.95}\cdot 0.45H_2O$	3.81	330
MnO_x-BA	$K_{0.041}MnO_{2.04}\cdot 0.35H_2O$	3.83	233

As a further test of the effect of the carboxylic acids on the nanoparticle formation, nitric acid was added in place of butyric acid in order to test the effect of pH using an inorganic acid. The carboxylic acids have a pH of 2.2-2.4, and nitric acid was used at a comparable pH. These materials more closely resembled the control materials (Figure 20); this indicates that the butyric acid itself, not the pH, has the largest influence on the formation of the hollow spheres.

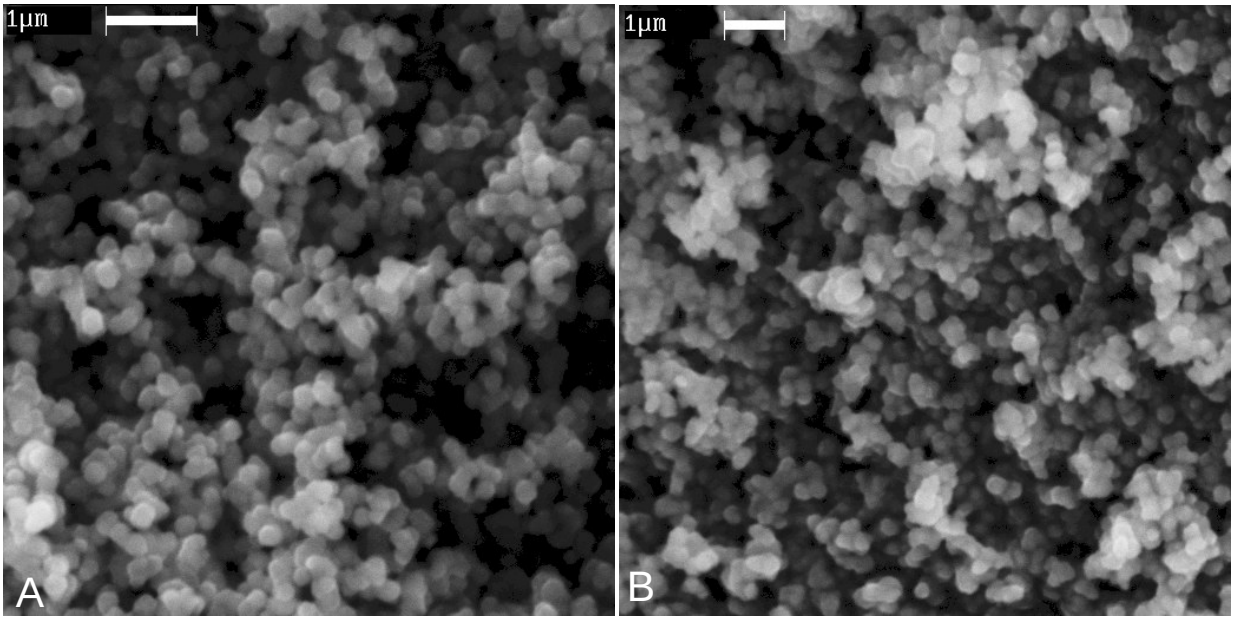

Figure 20. MnO_x synthesized in A) 0.1 M HNO_3 (pH 2) and B) 2.0 M HNO_3. Scale bar = 1 µm

A 10-fold excess of butyric acid is typically used in synthesis of the hollow spheres. Figure 21 shows the results of using higher concentrations of butyric acid. At a 15-fold excess (Figure 21A), the particles are still spherical though some of the monodispersity is lost. The particles are on average of comparable size to the hollow spheres synthesized with a 10-fold excess of BA. At a 20-fold excess (Figure 21B), however, while some of the particles are still spherical, the monodispersity is gone. Particles range from less than ⅓ µm, to 3 µm or more. The 30-fold synthesis product was very oily and unable to be retrieved from the filter frit.

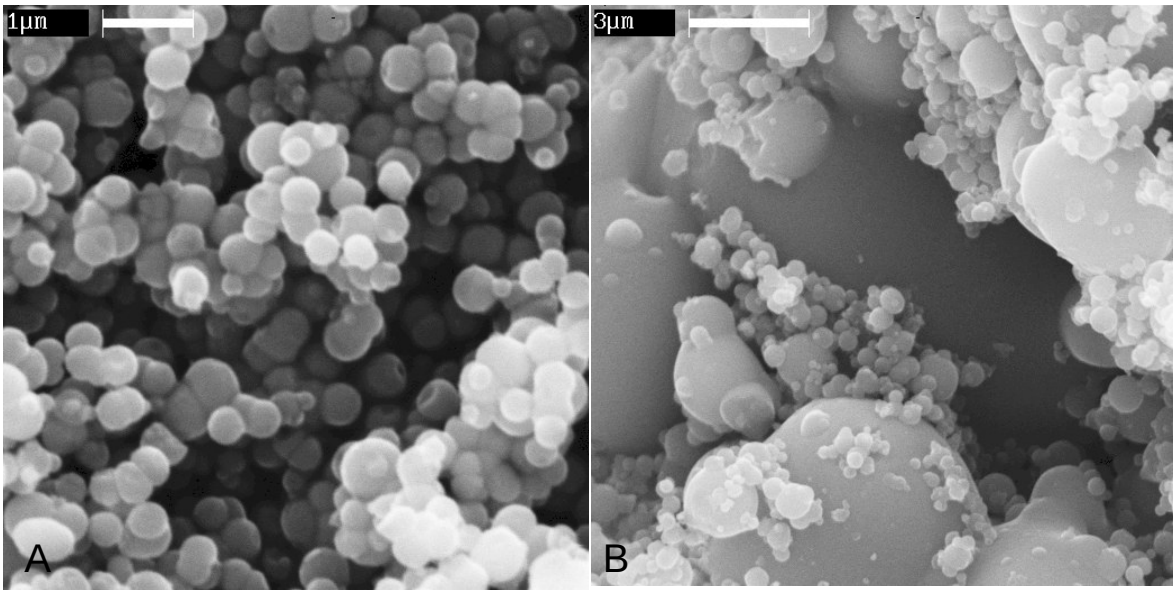

Figure 21. Manganese oxide synthesis with A) 15-fold BA and B) 20-fold BA. Scale bar = 1 µm

Doped Manganese Oxides

Manganese oxide nanoparticles are able to be isomorphously doped with a number of different transition metals. The metals chosen for this study were iron, copper and vanadium. Iron was chosen for its proximity to Mn in the periodic table, having a similar size and oxidation state as Mn, and has been shown to aid in the formation of hollow spheres in some hydrothermal systems.[54] It also is present in marine manganese nodules which show strong catalytic activity,[6] and has been synthesized in laboratories, giving promising catalytic results.[55-58] Vanadium is useful to examine as an early transition metal dopant, and has been seen to enhance the catalytic activity of manganese oxide systems.[59] Copper was also chosen due to its well-known ability to improve the catalytic activity of manganese oxides.[8,39,45,60-69] The properties and catalytic activity of these materials were investigated.

Iron-doped

Manganese oxide spheres were successfully doped with Fe^{2+} using $Fe(NH_4)_2(SO_4)_2 \cdot 6H_2O$ and $FeCl_2 \cdot 4H_2O$. Fe^{2+} was isomorphously doped throughout the spheres, without significantly changing the morphology of the control spheres (Figure 22). With $FeCl_2$ being more difficult to accurately measure due to being very hydroscopic however, $Fe(NH_4)_2(SO_4)_2$ was used for all further analyses. Fe^{3+} was also attempted, however the materials did not retain their spherical morphology and the approach was therefore abandoned (Figure 23).

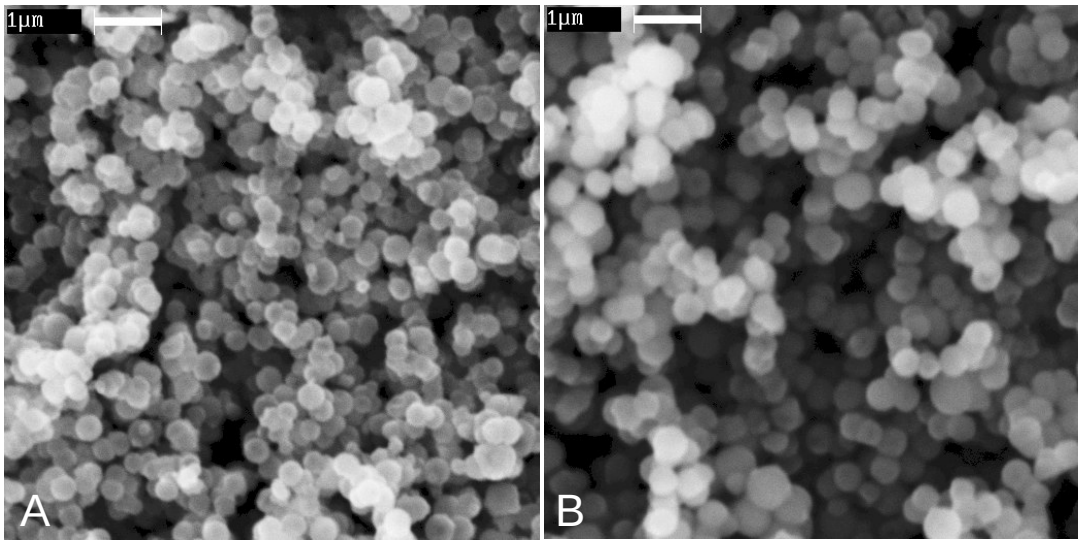

Figure 22. Fe^{2+}-doped MnO_x ($Fe_{0.35}MnO_x$). A) $FeCl_2$, B) $Fe(NH_4)_2(SO_4)_2$. Scale bar = 1 µm

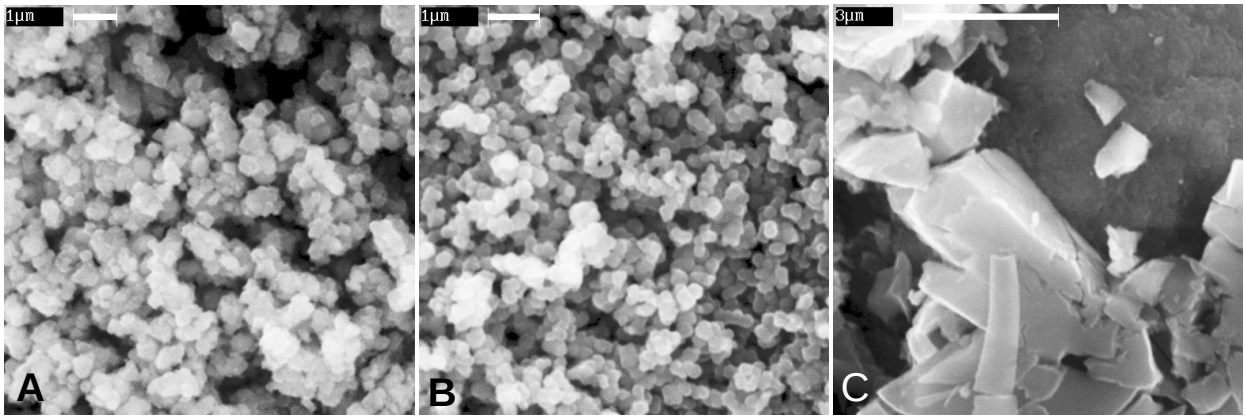

Figure 23. Fe^{3+}-doped MnO_x's: A) $FeCl_3$ ($Fe_{0.35}MnO_x$), B+C) $Fe(NO_3)_3 \bullet 9H_2O$ (B: $Fe_{0.05}MnO_x$, C: $Fe_{0.35}MnO_x$). A+B, scale bar = 1 µm. C, scale bar = 3 µm

Synthesis with $Fe(NH_4)_2(SO_4)_2$ was done with each of the stoichiometric ratios from Table 1. These materials generally retained a spherical morphology, with exception to high dopant levels of iron (Figure 24). Flame AA Spectroscopy was used to determine the approximate iron content relative to the manganese. These data (Table 11) show that up to an added 0.2:1 Fe:Mn ratio, the efficiency of incorporation of iron is very high and gives a predictable doping trend. At levels greater than 0.2:1 Fe:Mn, however, the doping efficiency of iron declines (Figure 25). Throughout the different ratios used in Table 11, the one which showed the greatest morphological difference was 0.39:1 (1:1 added), in which the product had lost all monodispersity and spherical morphology (Figure 24C).

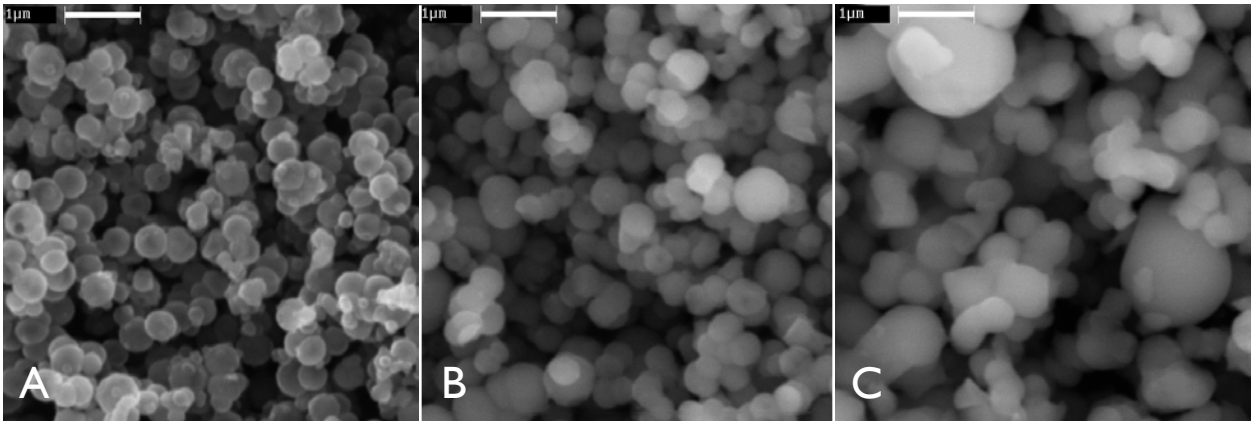

Figure 24. $FeMnO_x$-BA with $Fe(NH_4)_2(SO_4)_2$: A) $Fe_{0.05}MnO_x$, B) $Fe_{0.3}MnO_x$, C) $Fe_{0.39}MnO_x$. Scale bar = 1 µm

Table 11: Amount of iron added vs. incorporated into final product

Fe:Mn Added	Fe:Mn in Product
0.051	0.0505
0.083	0.077
0.11	0.0995
0.22	0.177
0.35	0.253
0.5	0.315
1.0	0.39

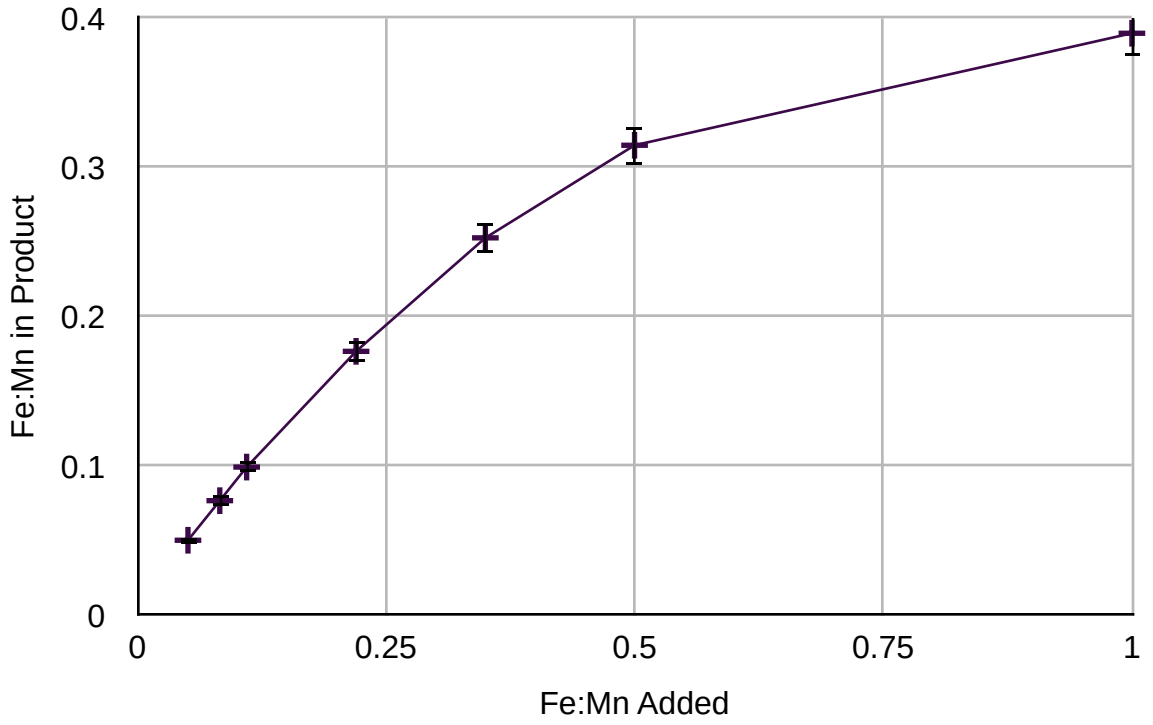

Figure 25. Graph showing incorporation of Fe into in MnO_x hollow spheres. Fe:Mn ratios were determined by atomic absorption

The $FeMnO_x$-BA materials exhibit a core-shell structure not seen in the un-doped MnO_x-BA. When analyzed by TEM, the iron-doped samples show cores inside their hollow shells. As the dopant level increases, the wall thickness of the shell increases until the sphere becomes solid (Figure 26). In $Fe_{0.18}MnO_x$-BA, many spheres have completely solidified with the exception of a single thick-walled core-shell structure (Figure 26C). At concentrations above 0.18:1 Fe:Mn, all spheres become solid (Figure 26D + 26E). The core-shell structures are present in the samples that are most efficiently doped (up to ca.0.2:1, Figure 25), and when the spheres solidify, the doping efficiency decreases. The average sphere size of the solid spheres increases from ca. 200 nm to 400-500 nm in diameter. The core-shell structures seen in these materials are formed by an unknown mechanism, though there have been reports of other core-

shell structures formed by Ostwald Ripening[38] and several-step aqueous precipitation reactions.[32] To this point, we do not know the function or significance of these cores. These structures are seen in our Cu- and V-doped materials as well.

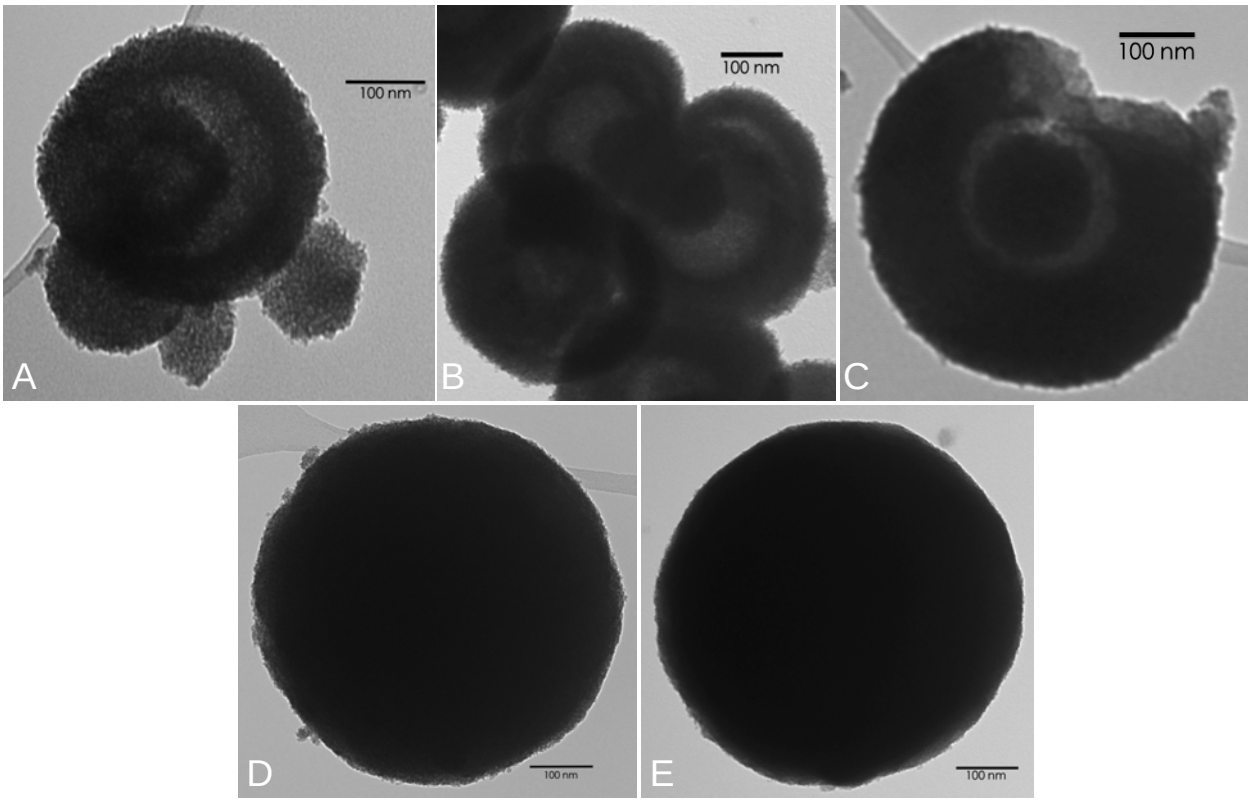

Figure 26. TEM images of $FeMnO_x$-BA core-shell structures:
A) $Fe_{0.05}MnO_x$, B) $Fe_{0.098}MnO_x$, C) $Fe_{0.18}MnO_x$, D) $Fe_{0.26}MnO_x$, E) $Fe_{0.33}MnO_x$.
Scale bar = 100 nm

The previous syntheses were done with stoichiometric ratios of Fe using balanced redox reactions (Table 1). The effect of adding iron in a non-stoichiometric manner was done, i.e. using an excess of manganese or an excess of iron. In this experiment, Fe was added with Fe:Mn ratios of 0.1 to 0.6, in 0.1 increments. An excess of manganese (0.1-0.3 Fe:Mn) results in little to no effect on the morphology of the material (Figure 27A-C). An excess in iron (0.4-0.6 Fe:Mn) causes a significant loss of

monodispersity (Figure 27D-F). Fe:Mn ratios were determined for each sample by Flame AA (Table 12). Figure 28 graphs Fe:Mn ratios of stoichiometric and non-stoichiometric doping. It is seen that an excess of iron in the synthesis in fact lowers the doping efficiency of Fe, while excess Mn has little to no effect.

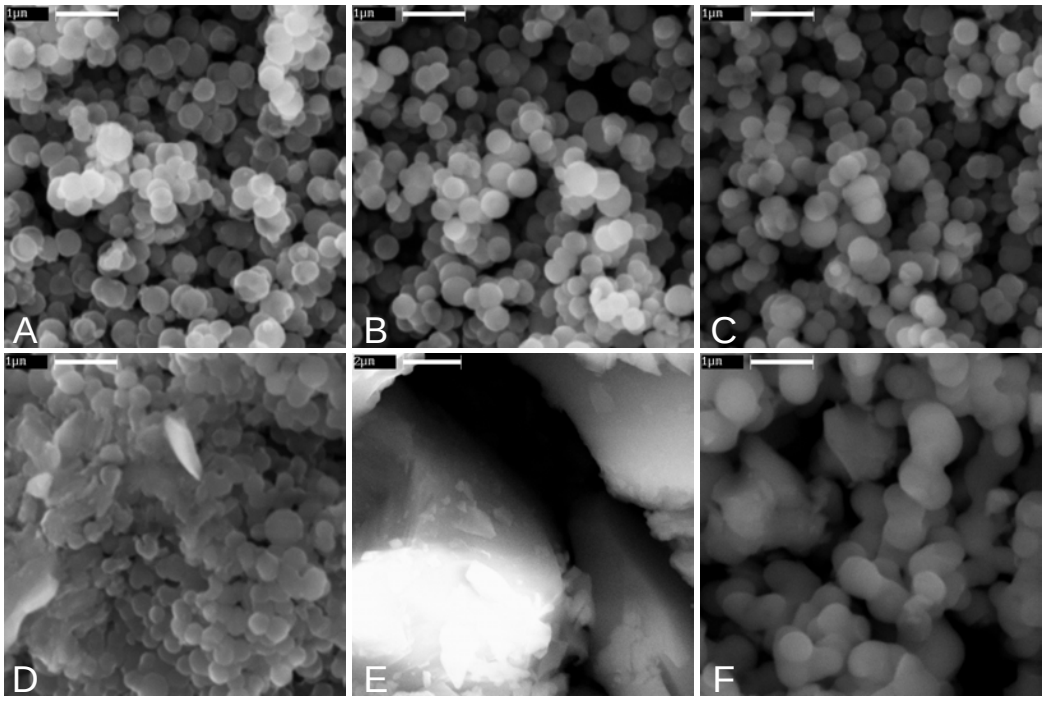

Figure 27. Non-stoichiometric synthesis products:
A) 0.1:1, B) 0.2:1, C) 0.3:1, D) 0.4:1, E) 0.5:1, F) 0.6:1 Fe:Mn. Scale bar = 1 µm

Table 12: Fe:Mn ratios added and in final product in non-stoichiometric syntheses

Fe:Mn Added	Fe:Mn in Product
0.1	0.0886
0.2	0.163
0.3	0.221
0.4	0.255
0.5	0.294
0.6	0.314

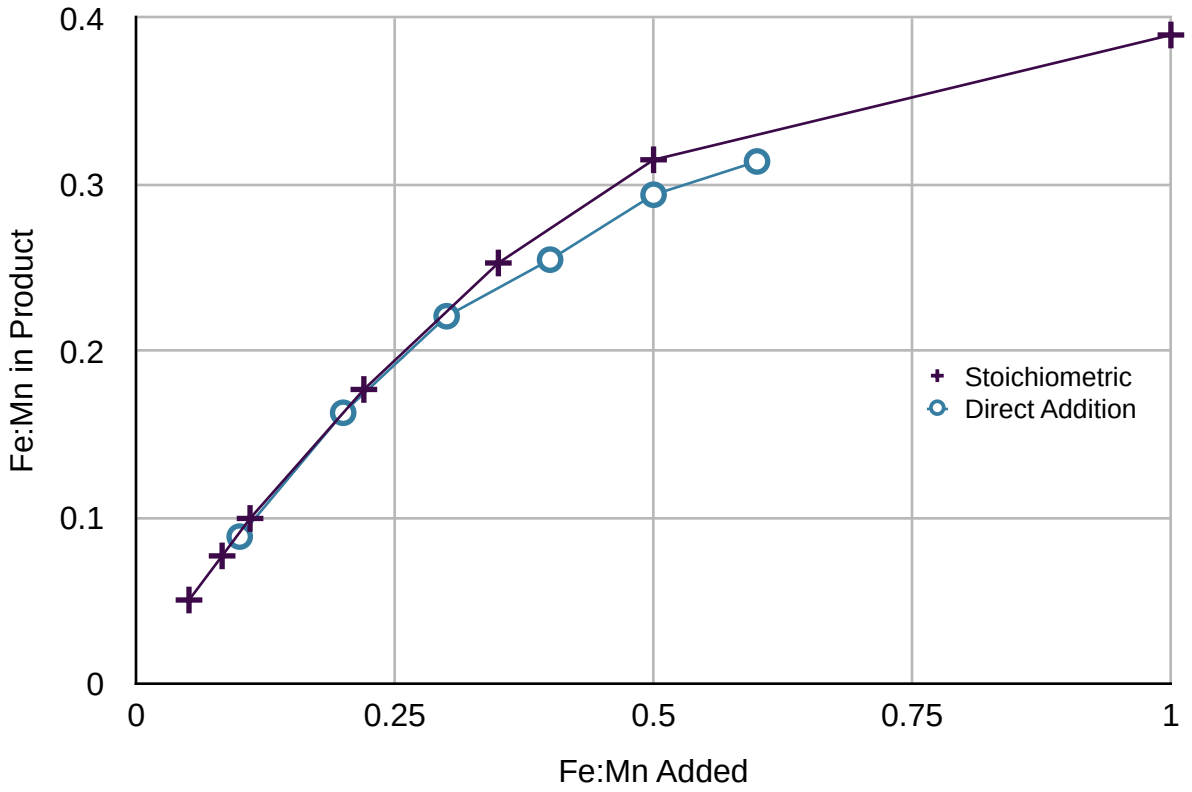

Figure 28. Fe:Mn ratios of stoichiometric vs. direct addition products

Three samples, $Fe_{0.092}MnO_x$-BA , $Fe_{0.17}MnO_x$-BA and $Fe_{0.26}MnO_x$-BA were analyzed for water content by TGA. With this information, the final molecular formula of these three samples was determined. The molecular formulas are shown in Table 13. Iron content has a positive correlation to oxygen and water content, and an inverse correlation to potassium content.

Table 13: Molecular formulas of $Fe_{0.092}MnO_x$-BA , $Fe_{0.17}MnO_x$-BA and $Fe_{0.26}MnO_x$-BA

Fe:Mn Added	Molecular Formula
0.1:1	$Fe_{0.092}MnO_{2.01}K_{0.0078}\cdot 0.62H_2O$
0.2:1	$Fe_{0.17}MnO_{2.06}K_{0.0032}\cdot 0.81H_2O$
0.35:1	$Fe_{0.26}MnO_{2.10}K_{0.0014}\cdot 1.06H_2O$

Iron was doped into samples synthesized with acetic and propionic acid ($FeMnO_x$-AA and $FeMnO_x$-PA, respectively), as well as the control sample ($FeMnO_x$-C). All samples had good incorporation of Fe, like the BA-derived MnO_x. The acid-treated syntheses resulted in dense, shiny black powders with nondescript morphologies (Figure 29A). The $FeMnO_x$-C (Figure 29B) resembled the MnO_x-C material. Iron content was determined by Flame AA (Table 14).

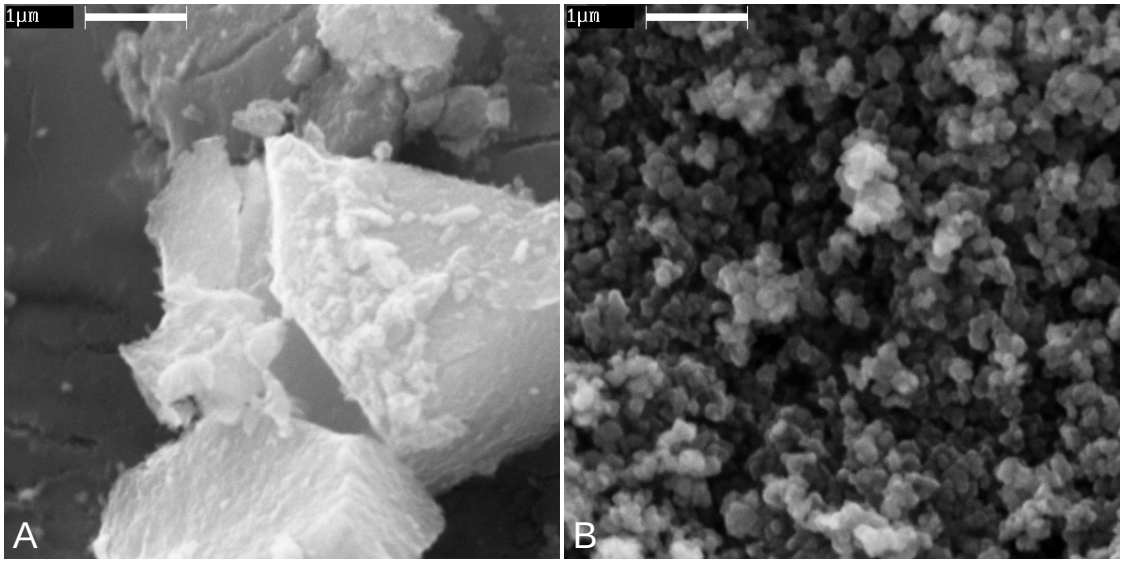

Figure 29. SEM Images of Fe-MnO_x A) AA/PA, B) Control. Scale bar = 1 µm

Table 14: Fe:Mn and K:Mn ratios of MnO_x-AA, -PA, -C samples

Acid Used	Fe:Mn Added	Fe:Mn in Product
Acetic	0.05	0.0459
Acetic	0.1	0.0968
Propionic	0.05	0.0453
Propionic	0.1	0.0961
None	0.05	0.0454
None	0.1	0.0968

The surface areas of the Fe-doped samples were acquired by BET surface area analysis (Table 15). The acid used appears to have little effect on the surface area at the lower concentrations of Fe. In the BA-treated samples, a clear trend can be seen where the surface area reaches a maximum at 0.18:1 Fe:Mn, then begins to decrease. The $Fe_{0.18}MnO_x$ sample, as mentioned above, are also the final core-shell structures before the efficiency of the iron-doping begins to decline with the formation of solid spheres. This indicates that the hollowness of the spheres as well as the core-shell structures have a strong effect on the surface area. When the spheres lose these features, i.e. become solid, their surface area begins to decline. With the solid spheres, the surface area decrease could be caused by the particles on the inside of the sphere not being accessible due to a loss of porosity throughout the sphere.

Table 15: Surface areas $FeMnO_x$-C, -AA, -PA and -BA

Acid Used	Fe:Mn	Surface Area (m^2/g)
Butyric	0.052	246
Butyric	0.078	295
Butyric	0.098	332
Butyric	0.18	434
Butyric	0.26	315
Butyric	0.30	265
Acetic	0.046	247
Propionic	0.45	241
None	0.45	260
None	0.097	313

Copper-doped

MnO_x materials were successfully doped with Cu^{2+} using $Cu(OAc)_2 \bullet H_2O$ ($CuMnO_x$-BA). The amounts of copper added and incorporated were determined by Flame AA (Table 16). These data show that the copper was incorporated with approximately 21% efficiency, however it incorporates in a very predictable, linear fashion (Figure 30). A reason it may incorporate less efficiently than iron could be the lower oxidation state of Cu relative to Fe, as well as it being smaller than Fe, and therefore has a greater size difference relative to Mn. These factors make Cu less comparable to Mn, and therefore it is harder to replace $Mn^{3/4+}$ ions with Cu^{2+} ions.

Table 16: Amount of copper added vs. in final product

Cu:Mn Added	Cu:Mn in Product
0.050	0.0157
0.10	0.0215
0.20	0.043
0.30	0.061
0.50	0.108
1.0	0.215

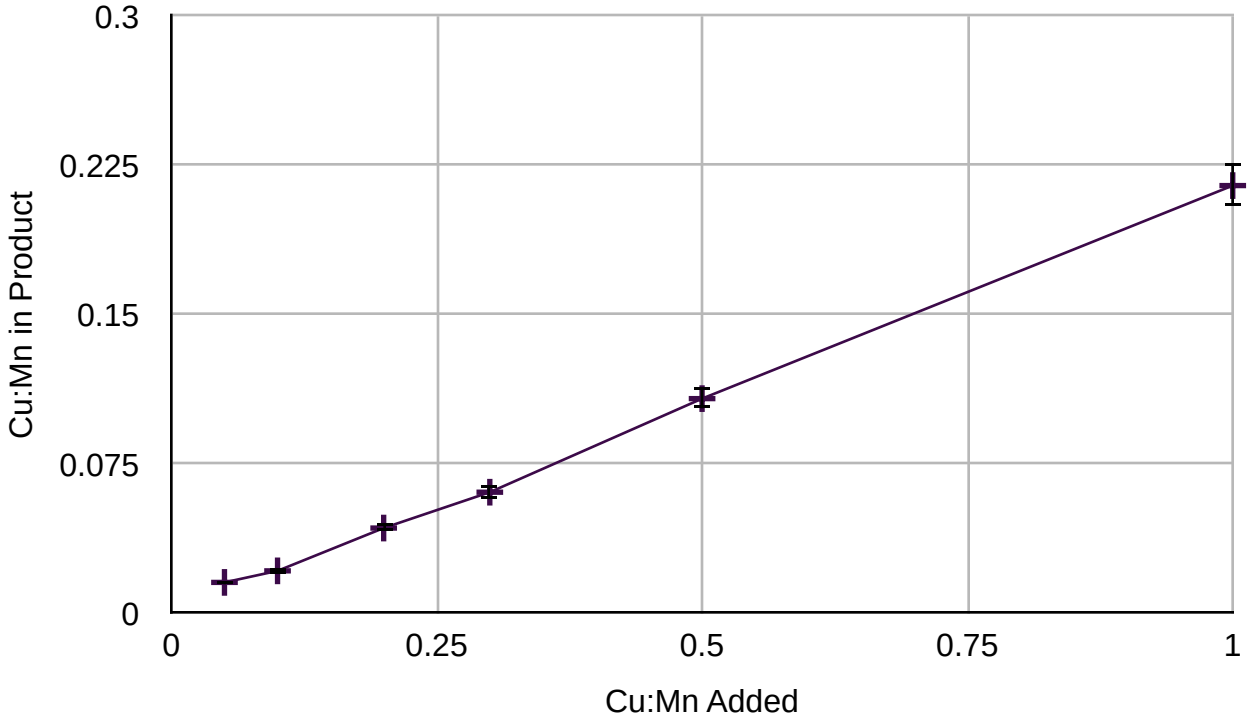

Figure 30. Graph showing incorporation of Cu into in MnO_x hollow spheres. Cu:Mn ratios were determined by atomic absorption.

SEM shows that the $CuMnO_x$-BA particles remain spherical at all dopant levels, though the size of the spheres increases as the concentration of copper increases (Figure 31). In these images, a few spheres can be seen as hollow by identifying what looks like a lysed cell (31B, middle-left). When analyzed by TEM (Figure 32), it can be seen that at all dopant levels, the spheres are in fact hollow. At lower dopant levels, the spheres adopt a core-shell structure (32A-B), which disappears at higher dopant levels (32C-F). This trend is unexpected since the undoped spheres lack a core-shell structure, while at low levels of Cu, a core is present and then as Cu levels are increased, the spheres become empty again. As with the Fe-doped materials, the significance and formation mechanism of the core-shell structure is yet to be determined.

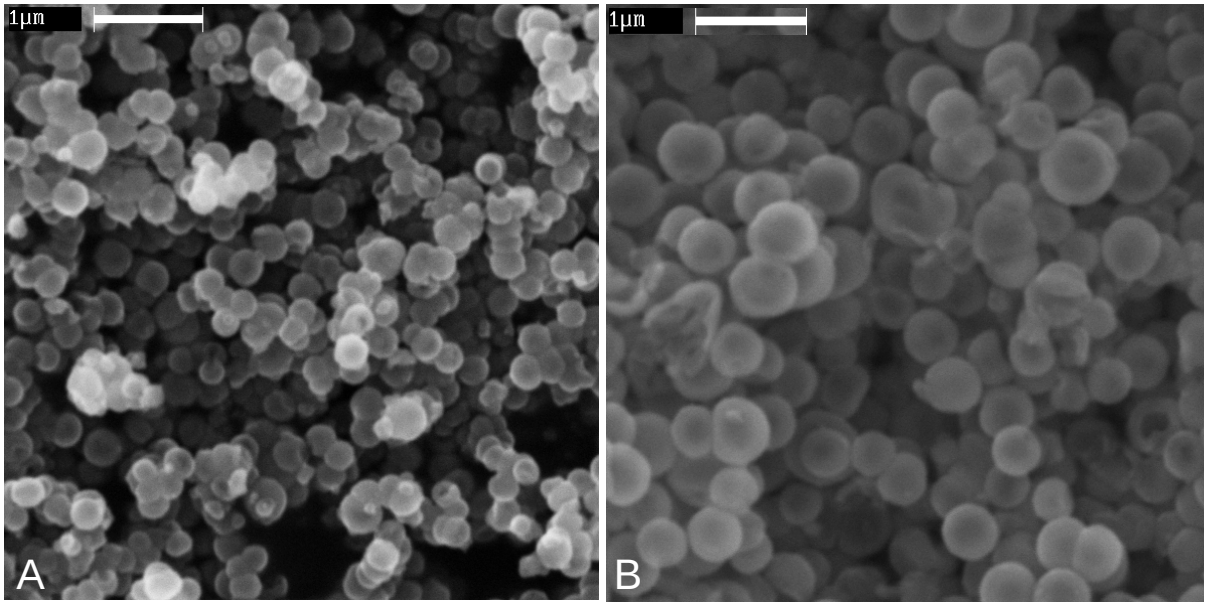

Figure 31. Cu^{2+}-doped MnO_x's with $Cu(OAc)_2$: A) $Cu_{0.016}MnO_x$, B) $Cu_{0.22}MnO_x$. Scale bar = 1 µm.

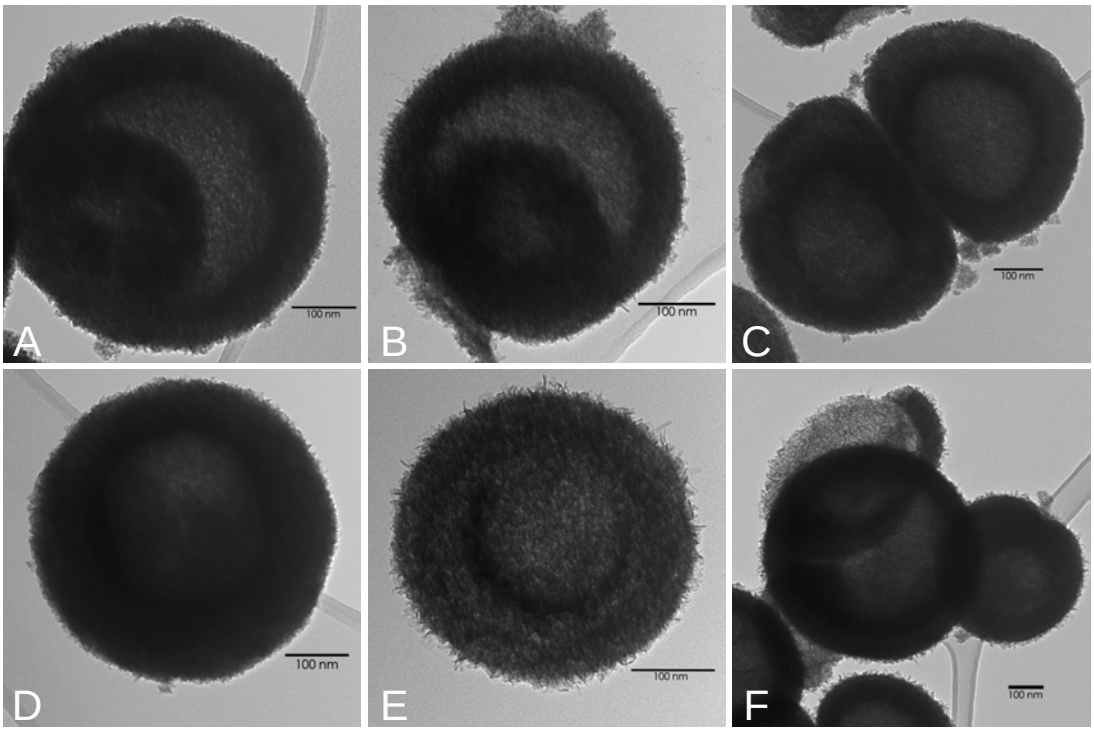

Figure 32. TEM images of $CuMnO_x$-BA:
A) $Cu_{0.014}MnO_x$, B) $Cu_{0.019}MnO_x$, C) $Cu_{0.04}MnO_x$,
D) $Cu_{0.059}MnO_x$, E) $Cu_{0.11}MnO_x$, F) $Cu_{0.21}MnO_x$. Scale bar = 100 nm

Three of the Cu-doped samples—$Cu_{0.024}MnO_x$, $Cu_{0.046}MnO_x$ and $Cu_{0.10}MnO_x$—were analyzed for water content by TGA. The final molecular formulas of these materials were determined (Table 17). There are no significant, consistent trends in H_2O, O or K amount as the copper dopant is increased. This suggests that the amount of potassium or of oxygen present, as well as waters of hydration, are not fully dependent on copper concentration.

Table 17: Molecular formulas of 0.1:1, 0.2:1 and 0.5:1 Cu:Mn samples

Cu:Mn Added	Molecular Formula
0.1	$Cu_{0.024}MnO_{1.86}K_{0.0017}\cdot 0.67H_2O$
0.2	$Cu_{0.046}MnO_{1.99}K_{0.0096}\cdot 0.64H_2O$
0.5	$Cu_{0.10}MnO_{1.76}K_{0.0030}\cdot 1.15H_2O$

Copper-doped samples were synthesized with acetic and propionic acid ($CuMnO_x$-AA, -PA), as well as a control with no acid ($CuMnO_x$-C). These samples (Figure 33) resemble the iron-doped samples which underwent the same treatment (Figure 29A), with nondescript morphologies and the acid-treated samples being dense, black shiny powders. Figure 33A is representative of all of the acid-treated samples. $CuMnO_x$-C has a morphology similar to that of the control though with a smaller particle size (Figure 33B). Copper amounts in these samples were determined by Flame AA and are shown in Table 18.

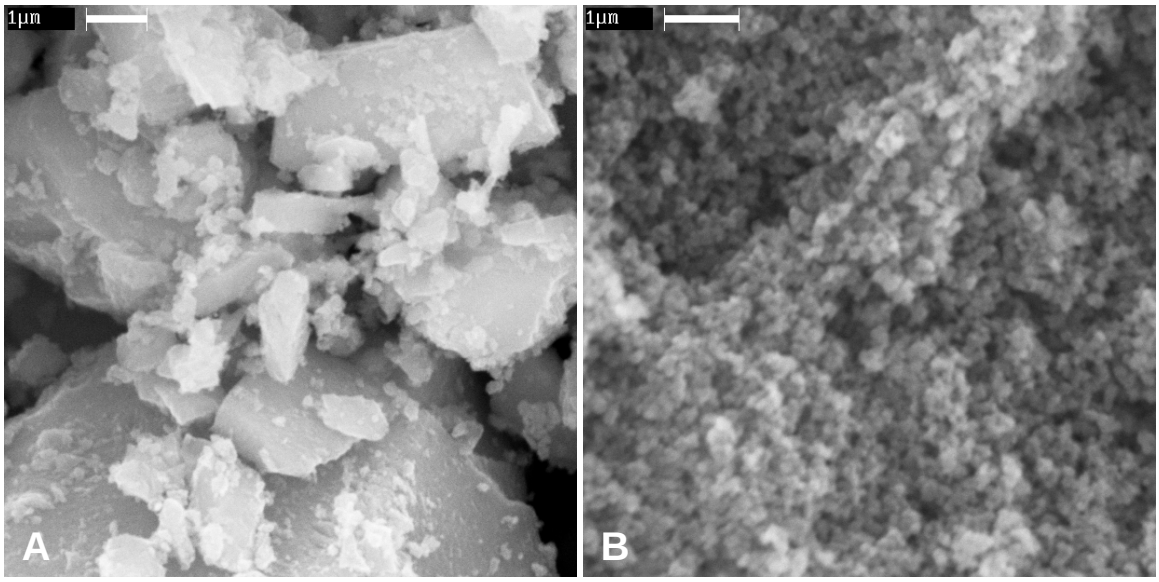

Figure 33. SEM images of A) $CuMnO_x$-AA/PA, B) $CuMnO_x$-C. Scale bar = 1 µm

Table 18: Cu:Mn ratios of AA/PA/non-acid—treated samples

Acid Used	Cu:Mn Added	Cu:Mn in Product
Acetic	0.5	0.149
Propionic	0.2	0.0571
Propionic	0.5	0.12
None	0.2	0.0837
None	0.5	0.181

Surface areas of several acid-treated Cu-doped samples were acquired by BET surface area analysis, as well as the two control samples (Table 19). The surface areas are relatively high for $CuMnO_x$-AA, and are comparable to the $FeMnO_x$-PA and $FeMnO_x$-C surface areas for $CuMnO_x$-PA and $CuMnO_x$-C. There is no definite trend for surface area to amount of Cu in the samples. The surface area appears to level out at $Cu_{0.11}MnO_x$-BA.

From previous measurements, the un-doped hollow spheres have 233 m^2/g. The carboxylic acids all appear to have a positive effect on the surface area to MnO_x-C, which has a surface area of 133 m^2/g.[39] In the control Cu-doped samples, the presence of Cu increases the surface area to that of MnO_x-BA, even in the absence of any carboxylic acids. This means that copper either increases the porosity of the spheres, or aids in reducing the particle size even further.

Table 19: Surface areas of $CuMnO_x$-AA, -BA, -PA and -C

Acid Used	Cu:Mn	Surface Area (m^2/g)
BA	0.014	301
BA	0.019	291
BA	0.040	251
BA	0.064	266
BA	0.11	321
BA	0.22	327
AA	0.084	350
AA	0.15	326
PA	0.16	237
None (C)	0.084	287
None (C)	0.18	255

Vanadium-doped

MnO_x materials were doped with vanadium using Na_3VO_4 ($VMnO_x$). The syntheses were done with 0.025:1, 0.05:1, 0.1:1, 0.2:1 and 0.3:1 V:Mn ratios in the synthesis. All dopant levels had comparable morphologies and particle sizes (Figure 34). The spherical morphology of the particles is retained with the incorporation of vanadium. TEM images show that core-shell structures are present, the cores of which appear to gradually diminish as the concentration of V is increased (Figure 35). At the lower concentrations (Figure 35A), the cores are scarcely present. As V increases, the cores increase in frequency before they begin to dissipate (Figure 35D). This unusual trend is similar to that seen in the Cu-doped spheres. The cause and significance of it is unknown.

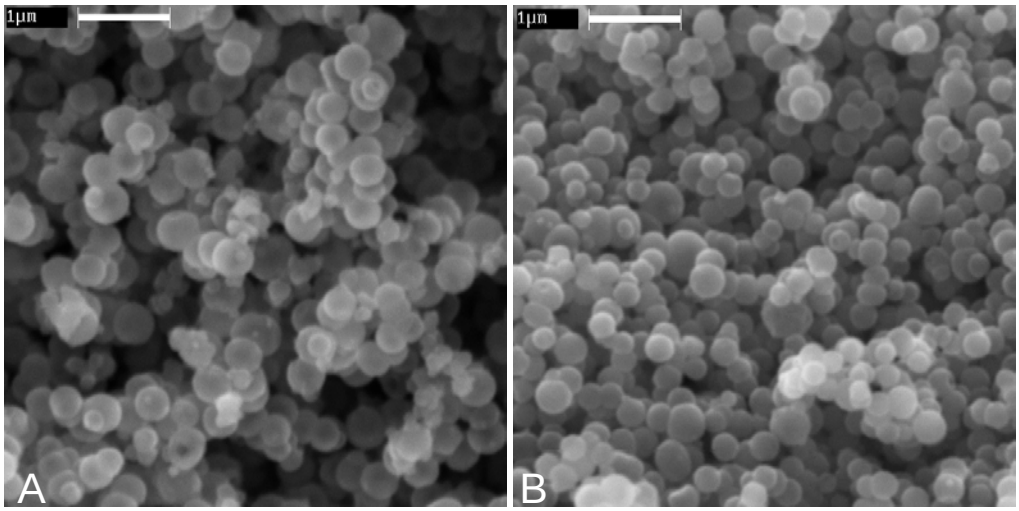

Figure 34. SEM images of $VMnO_x$-BA: A) $V_{0.021}MnO_x$, B) $V_{0.17}MnO_x$. Scale bar = 1 µm

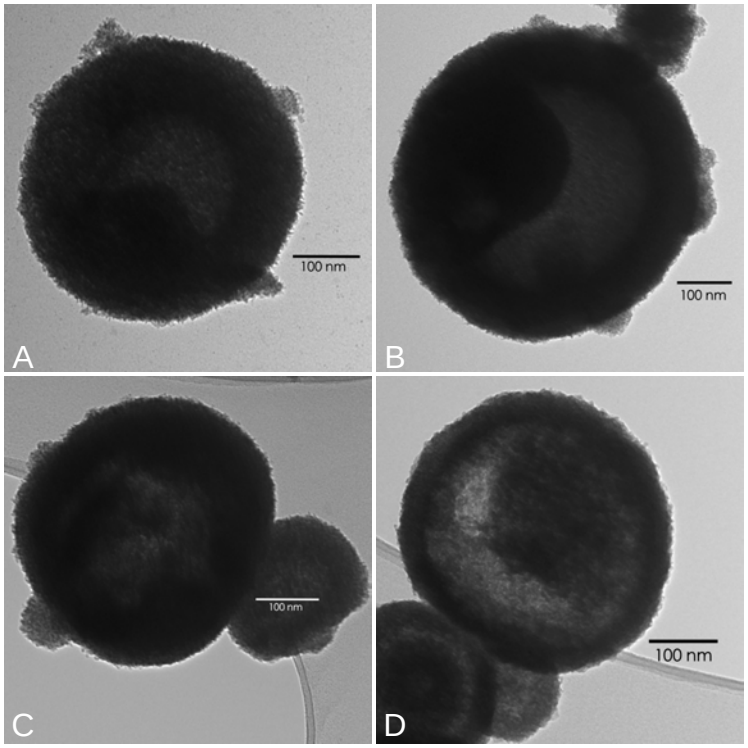

Figure 35. TEM images of $VMnO_x$-BA:
A) $V_{0.021}MnO_x$, B) $V_{0.038}MnO_x$, C) $V_{0.088}MnO_x$, D) $V_{0.16}MnO_x$. Scale bar = 100 nm

The vanadium amounts in the products were determined by Flame AA (Table 19). The vanadium does not efficiently add into the materials, however it is reliable enough to still see a general positive trend. Error margin is ±10 % for each value.

Table 20: Amount of V added vs. amount in final product

V:Mn Added	V:Mn in Product
0.025	0.021
0.05	0.038
0.1	0.075-0.088
0.2	0.14-0.16
0.3	0.16-0.18

Surface area analysis of $VMnO_x$-BA samples initially show a sharp increase in surface area as the V concentration increases, followed by a drop off in surface area as the concentrations approach what appears to be the maximum dopant level of approximately 0.2:1 (Table 21).

Table 21: BET surface area measurements of $VMnO_x$

V:Mn	Surface Area (m^2/g)
0.021	295
0.038	331
0.088	306
0.16	267
0.17	237

Copper and Iron double-doped

$FeMnO_x$ materials displayed the highest surface areas (up to 434 m^2/g), while Cu is known to increase catalytic activity.[15,44,45] In an attempt to optimize both, Cu^{2+} and Fe^{2+} were added together into the synthesis in varying amounts ($CuFeMnO_x$-BA, ranging from low copper and high iron, to high copper and low iron. Amounts of copper and iron added and in the final product were determined by Flame AA (Table 22). As the amount of Fe increases, the efficiency of Cu-doping decreases. At high concentrations of both Fe and Cu, the doping efficiency of both decreases. At lower concentrations of Fe, the spheres remain monodisperse, while as Fe content is increased, the monodispersity is lost (Figure 36).

Table 22: Amount of Cu and Fe added vs. amount in final product

Fe:Mn Added	Cu:Mn Added	Fe:Mn in Product	Cu:Mn in Product
0.051	0.30	0.048	0.041
0.051	1.0	0.050	0.19
0.11	1.0	0.088	0.16
0.22	1.0	0.15	0.14
0.22	0.50	0.20	0.029
0.22	0.30	0.20	0.063

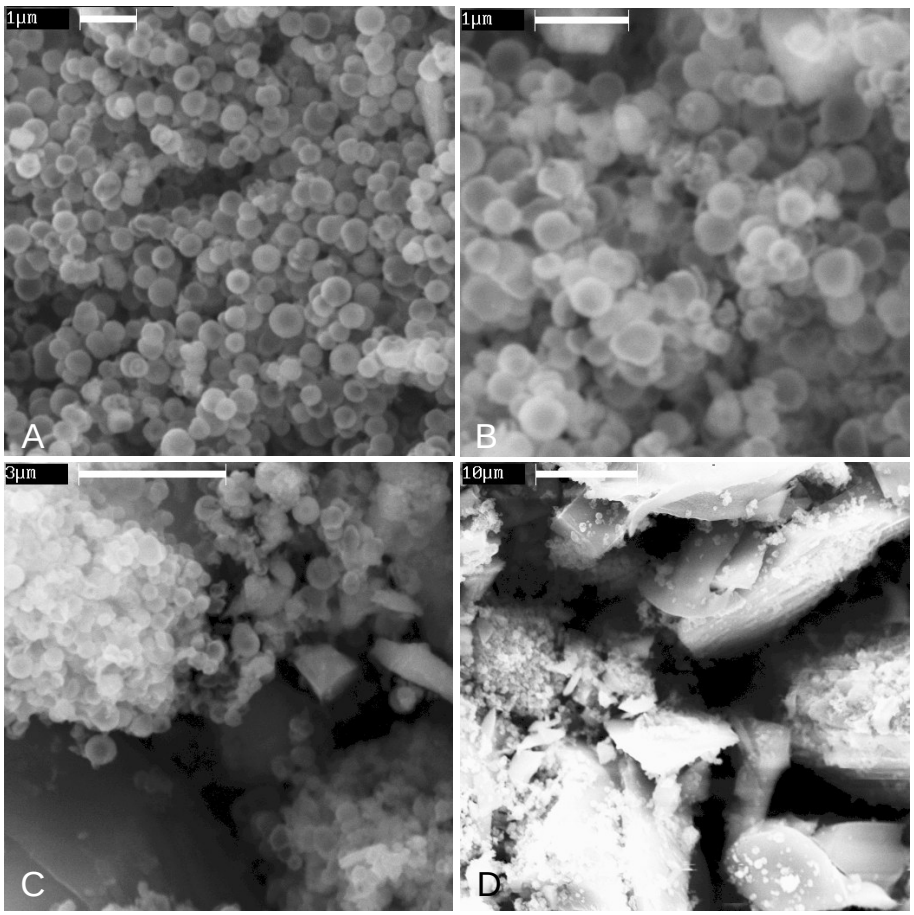

Figure 36. A) $Cu_{0.19}Fe_{0.050}MnO_x$, B) $Cu_{0.16}Fe_{0.088}MnO_x$, C) $Cu_{0.14}Fe_{0.15}MnO_x$, D) $Cu_{0.041}Fe_{0.048}MnO_x$. Scale bar = 1 µm (A+B), 3 µm (C) and 10 µm (D)

The water content of these materials was determined by TGA, and their molecular formulas were determined (Table 23). As total dopant level increases the amount of H_2O increases, while the amount of O decreases due to the average ox. state of metal decreasing, with $Fe^{2+/3+}$ and Cu^{2+} replacing $Mn^{3+/4+}$. The decrease in oxygen is likely due to the inability of Cu or Fe to adopt the 4+ oxidation state that manganese has, thus reducing the amount of oxygen that can be incorporated.

Table 23: Molecular formulas of $CuFeMnO_x$

Cu:Fe:Mn	Molecular Formula
0.025 : 0.18 : 1	$Cu_{0.025}Fe_{0.18}MnO_{1.51}\cdot 1.73H_2O$
0.2 : 0.05 : 1	$Cu_{0.2}Fe_{0.05}MnO_{1.29}\cdot 1.92H_2O$
0.14 : 0.14 : 1	$Cu_{0.14}Fe_{0.14}MnO_{1.26}\cdot 3.04H_2O$

Catalysis

Manganese oxides work as oxidative catalysts for several reactions, including the conversion of alcohols to carbonyls, CO to CO_2 and the total oxidation of organics, among others. They are presumed to react by the Mars van Krevelen mechanism (Figure 5).[9,12-18] Depending on the metal dopant or other reaction conditions, the catalytic activity varies. In this first reaction, a CO molecule picks up an oxygen from the manganese oxide, forming CO_2. The oxygen is then replaced by atmospheric O_2, thus reforming the catalyst (Figure 37). This is a form of the Mars van Krevelen mechanism as well.

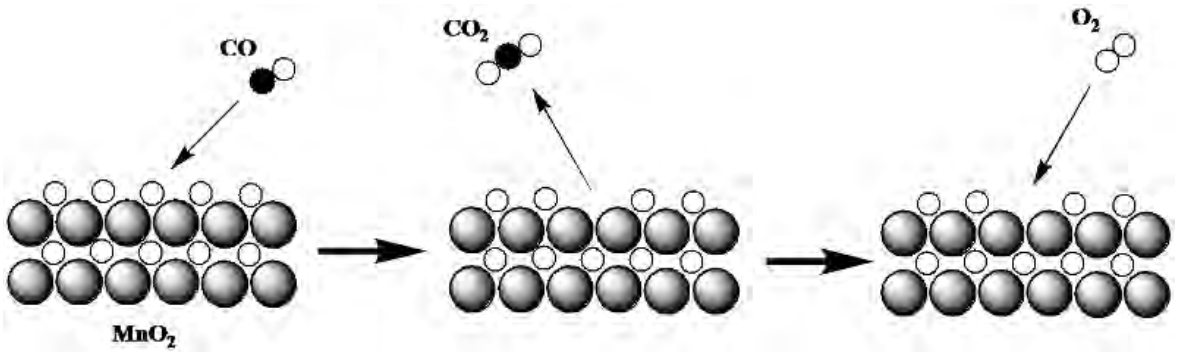

Figure 37. Oxidation of carbon monoxide by the Mars van Krevelen mechanism[25]

The catalytic activity for CO oxidation was tested using a fixed-bed gas flow reactor (Figure 16). The catalytic activity of $Fe_{0.092}MnO_x$-BA, $Cu_{0.016}MnO_x$-BA and $V_{0.075}MnO_x$BA were determined (Table 24). $Cu_{0.016}MnO_x$-BA showed the highest catalytic activity at low temperatures, with 15% of CO being converted to CO_2 at 25° C, while $Fe_{0.092}MnO_x$ only converted 4% at 25° C, and $V_{0.075}MnO_x$ converted 0%.

Table 24: Catalytic activities of Fe, Cu and $VMnO_x$-BA samples

Temperature (° C)	% CO to CO_2 ($Fe_{0.092}MnO_x$)	% CO to CO_2 ($Cu_{0.016}MnO_x$)	% CO to CO_2 ($V_{0.075}MnO_x$)
25	4	15	0
50	9	19	—
100	21	56	9
150	55	100	25

The manganese oxide materials were also tested for their ability to convert isopropanol to acetone by the mechanism in Figure 5, using a tube furnace setup (Figure 15). The catalytic activities have shown both Fe and Cu corresponding to high

catalytic conversions, with V reducing the catalytic activity of the materials (Table 25). Compared to the un-doped spheres, however, there is little significant catalytic improvement with the Fe- and Cu-doped materials. In the double-doped systems, the catalytic efficiencies dropped relative to the efficiencies seen with only one of the metals present (Table 26), and the presence of higher amounts of Fe decreases the catalytic efficiency more than the presence of high levels of Cu. Trends of catalytic activities at 250° and 200° C are shown in Figure 38 and 39 for single-doped systems. At 200° C, the amount of each dopant is inversely proportional to the catalytic activity, while at 250° C, until higher dopant levels, the catalysis is high, being in the 90-100% range. At 250° C, low amounts of Cu appear to hurt the activity, while 0.04:1 Cu:Mn and above increases the efficiency to almost 100%, while an increase in Fe eventually becomes deleterious to the materials' catalysis. The majority of our catalytic results for the Cu-doped materials are in agreement with other reports of copper aiding in the catalytic activity of manganese oxides,[60-69] however the V-doped catalysis results would be expected to be greater than or comparable to that of the control spheres. Fe-doped materials have been shown to increase catalytic activity as well,[55-58] however this was only seen in our materials at lower concentrations of Fe. With higher Fe levels, the materials undergo morphological changes that seem to hurt their catalysis as well.

These results, compared with those for CO oxidation, imply that the copper-doped materials may prove to be the strongest catalysts at lower temperatures. However with the temperatures currently used for isopropanol oxidation, that cannot be said for certain. Lower temperatures have yet to be tested.

Table 25: Catalytic activities of various MnO_x materials

Metal Dopant	Dopant to Mn Ratio	% Conversion at 200° C	Metal Dopant	Dopant to Mn Ratio	% Conversion at 250° C
Cu	0.06	76	Cu	0.015	60.44
Cu	0.11	84.14	Cu	0.019	68.06
Cu	0.015	91.61	Cu	0.04	91.58
Cu	0.021	88.47	Cu	0.06	91.25
Cu	0.040	85.38	Cu	0.11	97.77
Cu	0.21	71.89	Cu	0.21	98.68
Fe	0.054	95.61	Fe	0.052	94.24
Fe	0.20	70.61	Fe	0.20	90.69
Fe	0.24	62.09	Fe	0.24	53.62
V	0.08	59.75	V	0.08	64.19
V	0.16	48.07	V	0.16	73.33
None	None	91.94	None	None	88.94

Table 26: Catalytic activities of $CuFeMnO_x$ materials

$CuFeMnO_x$	% Conversion at 200° C	% Conversion at 250° C
$Cu_{0.04}Fe_{0.05}MnO_x$	75.01	90.27
$Cu_{0.03}Fe_{0.18}MnO_x$	47.55	73.00
$Cu_{0.2}Fe_{0.05}MnO_x$	79.65	95.59
$Cu_{0.14}Fe_{0.14}MnO_x$	50.71	90.08

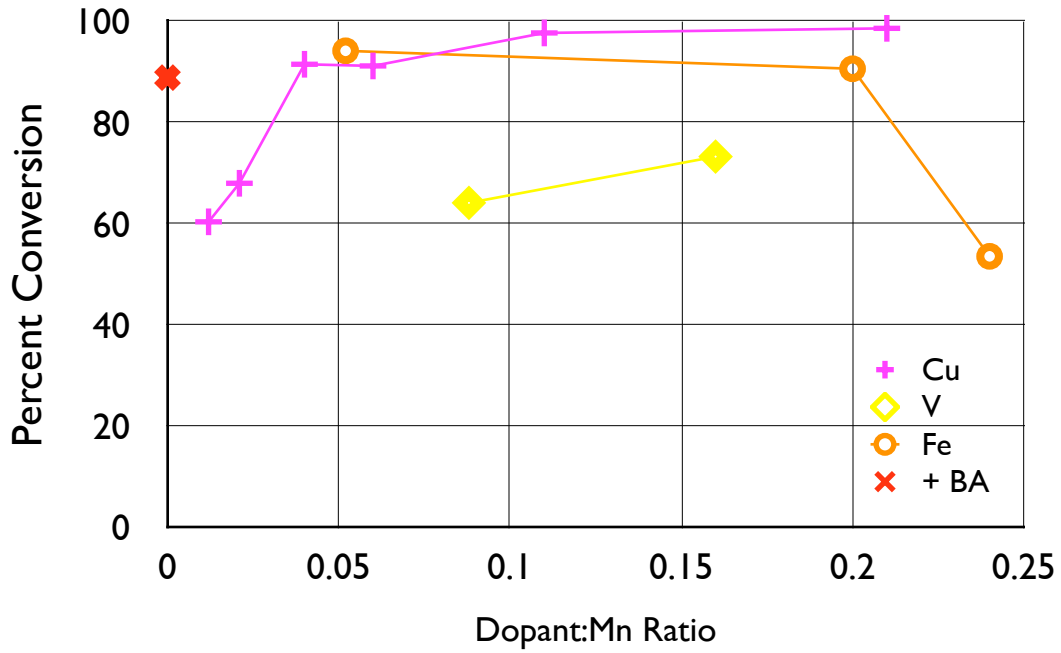

Figure 38. Conversion percents of various doped and un-doped MnO_x's at 250° C

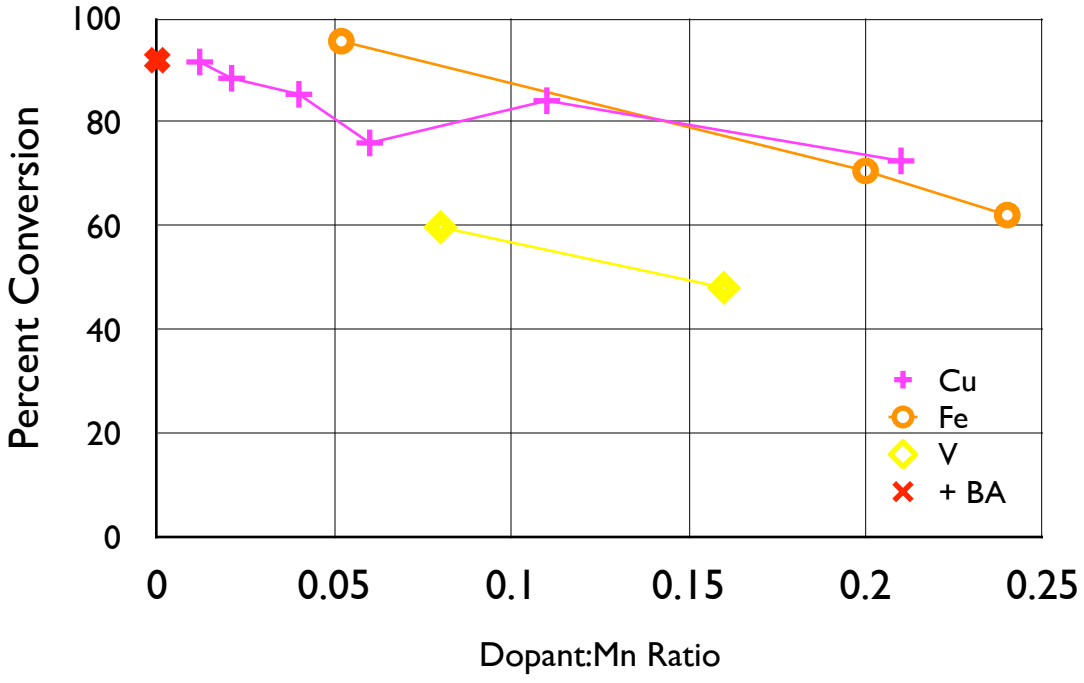

Figure 39. Conversion percents of various doped and un-doped MnO_x's at 200° C

Conclusion

In summary, I have successfully incorporated several transition metals into manganese oxides, and found the effects of different concentrations of iron, copper and vanadium on the morphology, surface area and catalytic ability of the nanostructured manganese oxides. Iron-doping tends to form core-shell structures at low concentrations of iron, which gradually become solid spheres as the concentration increased. Copper provides the strongest enhancement of catalytic ability for CO oxidation, yet is comparable to iron for isopropanol oxidation. In the presence of acetic acid in place of butyric acid in the initial solution, copper dopants cause the surface areas to increase by over 100 m^2/g, although the materials are no longer brown spheres but hard, black, non-descript rock-like structures.

Fe^{2+} and Cu^{2+} both are efficiently and predictably incorporated into the structure of the manganese oxides as they precipitate. Up to 0.2:1 Fe:Mn ratios, iron is almost completely incorporated into the product. Copper is incorporated in a linear fashion as concentrations increase, with 20-25% of the added copper being incorporated into the material. Vanadium is not efficiently incorporated in, due to large variations in the amount that can be added in with different trials. The doping ability of vanadium is fairly inconsistent.

When added together, Cu and Fe reduce the catalytic activity of the samples, yet the strongest decline is seen in the samples with a higher iron content, showing that it has a particularly negative effect when combined with copper. The surface areas of these materials are still yet to be determined.

Future Directions

One logical next step in the search for an efficient catalysts is to investigate the catalytic conversion of different alcohols such as 2-butanol. Lower temperature catalysis will be implemented as well, as a catalyst is more favorable if it can function at lower temperatures. The surface areas of the double-doped systems is yet to be determined, as well as several other dopant levels of both iron and copper.

An important experiment that should be tested in the future is to measure the quantity of Lewis and Brønsted acid sites on the material by using the pyridine adsorption technique.[70] In this method, pyridine is added to the sample under vacuum, adsorbing onto the surface at both the Lewis and the Brønsted acid sites. When the pyridine binds onto a Lewis acid site, it stays as pyridine, yet when it bonds to a Brønsted site, it becomes a pyridinium ion. When subsequently analyzed under IR, the pyridine and pyridinium both absorb at different frequencies, and the ratio of the two can be quantified by integrating the spectrum under each peak. This can provide valuable information on the mechanism of oxidation utilized by these catalysts.

One other experiment which could provide valuable information is doping the materials with iron in order to increase the surface area, while depositing copper on the surface of the material by *incipient wetness*.[71] In this method, a heterogeneous catalyst is created, but in two different phases. The manganese oxide is initially prepared separately. A salt of the desired metal is then dissolved, and the manganese oxide is added to the salt solution. The metal ions are pulled into the structure resulting in a material with the metal on the structure, as opposed to being incorporated directly into the crystalline structure. Copper has been seen to enhance the catalytic activity of

materials added by this method, so if the surface area of the materials were increased (Fe-doped have been seen to give up to 434 m^2/g), then the catalytic improvement with the copper present on the surface could be dramatically increased.

Appendices

Appendix 1

Polyvinylpyrrolidone and polyethylene glycol

Hollow spheres can be very valuable due to potential biological applications including encapsulation of drugs or other biologically relevant compounds.[72-74] With the proposed formation mechanism of the hollow spheres, attempts were made to trap a molecule inside the hollow spheres by finding something that is more soluble in butyric acid emulsions than in H_2O, while being large enough to be trapped when the hollow spheres formed. Materials that were hoped to demonstrate this were polyvinylpyrrolidone (PVP, avg. molecular weight = 8,000 g/mol) and polyethylene glycol (PEG, avg. molecular weight = 10,000 & 20,000 g/mol). The polymers were dissolved with the $MnSO_4$ and the manganese oxides were synthesized in the presence and absence of BA (Figure 22A), all of which seemed to lose their spherical morphology. Once the final materials were formed, a KBr pellet containing each material was made and and IR spectrum was acquired to detect the presence of any organics present. No organics, however, were detected in any of the samples. Figure 22B is representative of the spectrum of all samples.

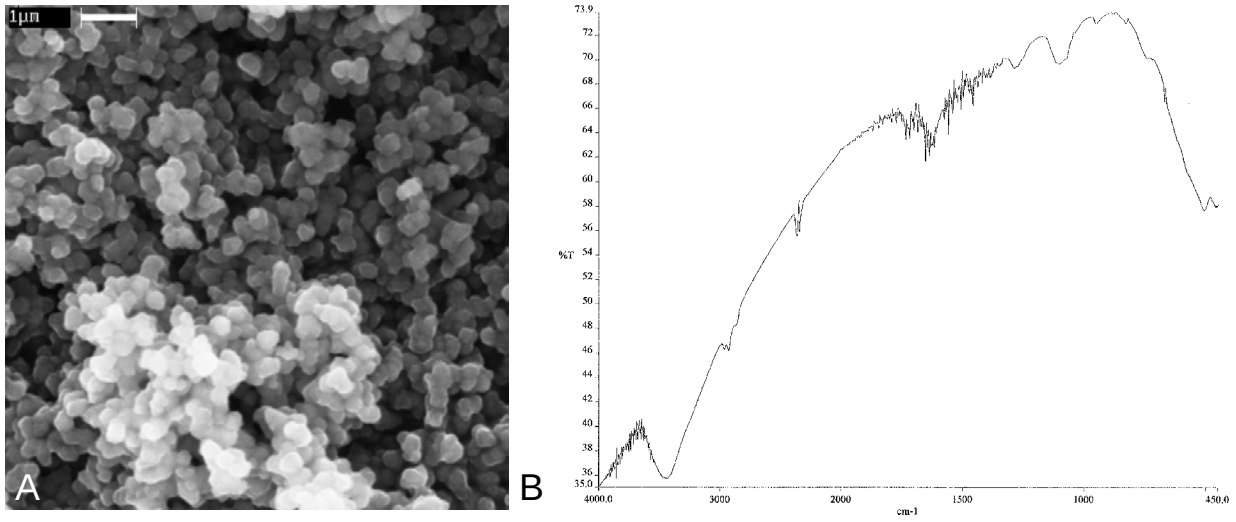

Figure 40. Synthesis with PVP and PEG: A) SEM image representative of all samples (scale bar = 1 µm), B) FT-IR spectrum

Appendix 2

<u>MnO_x hollow spheres as templates for TiO_2</u>

Manganese oxides supported on TiO_2 have been seen to enhance activity in oxidation systems.[75,76] To be more cost-effective, MnO_x materials were coated with a film of titanium dioxide ($TiMnO_x$) as opposed to MnO_x materials being supported on TiO_2 particles. These materials showed little morphological variation from the regular hollow spheres (Figure 41). This is because the BA-treated hollow spheres were used as a template for the TiO_2 shell to form on, which should not change the morphology of the material. The initial hollow spheres were dried at 110° C and at room temperature for comparison. Flame AA confirmed the presence of Ti in the sample, the RT-dried sample having 0.54:1 Ti:Mn and the oven-dried sample with 0.18:1 Ti:Mn.

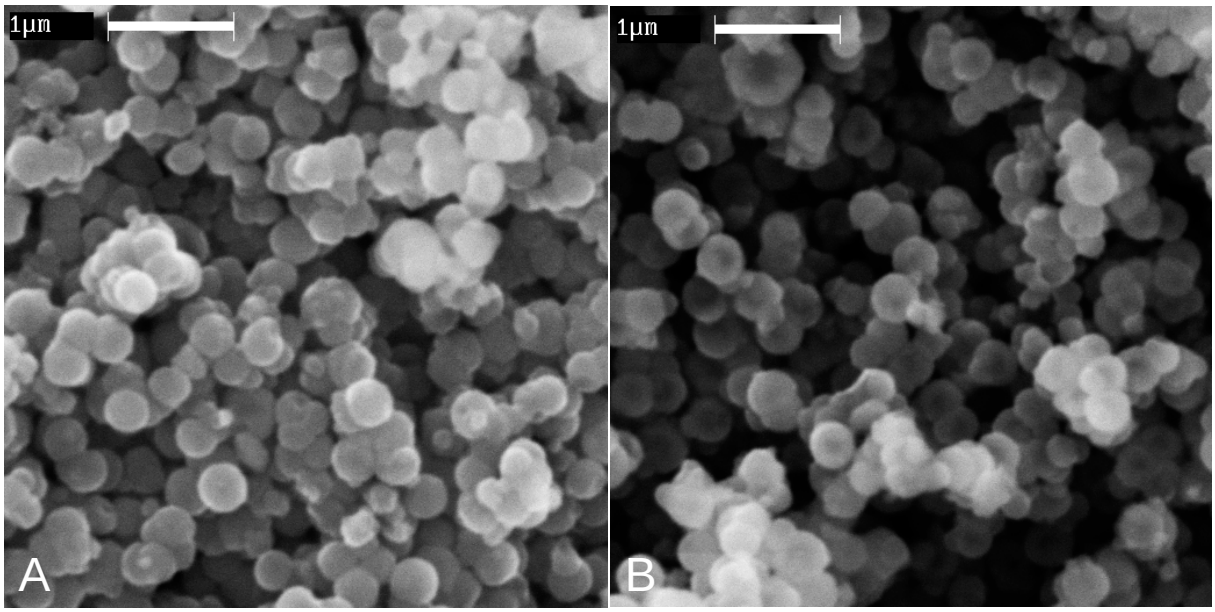

Figure 41. $TiMnO_x$ made using: A) RT-dried MnO_x, B) 110° C-dried MnO_x. Scale bar = 1 µm

Appendix 3

DMSO/DMF/acetonitrile in H_2O as solvent

Butyric acid forms emulsions in water due to the differences in polarity between the acid and the solvent, water. To see the effect of altering this, the polarity of the reaction solvent was lowered by combining water with dimethyl sulfoxide (DMSO), dimethylformamide (DMF) and acetonitrile. DMSO was used in syntheses with and without the addition of butyric acid. All of these materials have particularly small particle sizes (Figure 42), however butyric acid appears to still have a structure-directing effect on the particles due to the relatively larger particle size (42C-D).

BET surface area analysis was done on the 10% DMSO sample w/ BA. A surface area of 128 m^2/g was determined, which is very close to that of the control *without* BA (133 m^2/g), yet less than half of the hollow spheres (285 m^2/g).

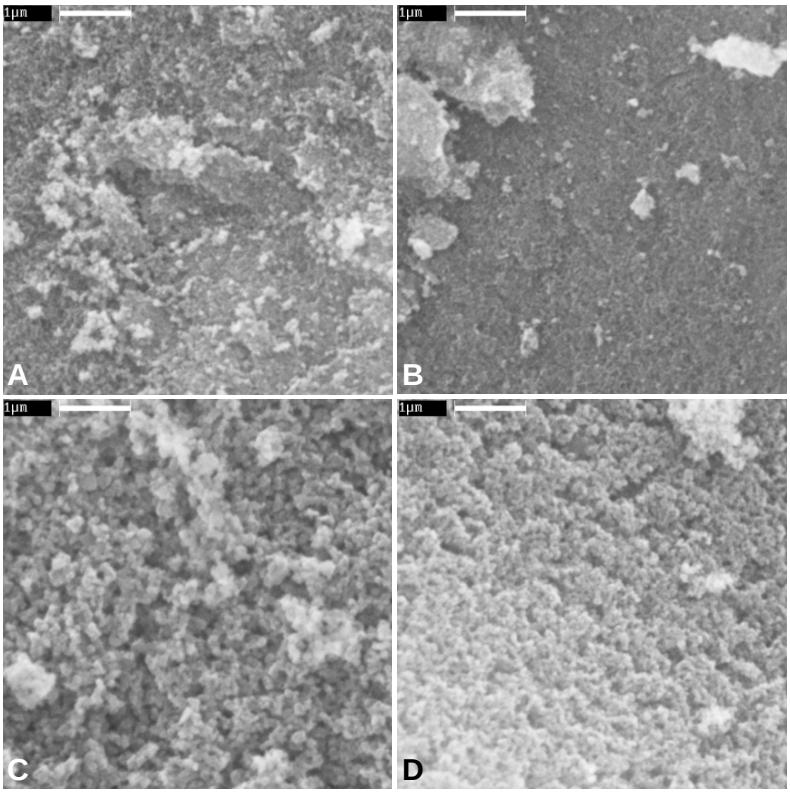

Figure 42. 10% DMSO w/o BA, B) 25% DMSO w/o BA, C) 10% DMSO w/ BA, D) 25% DMSO w/ BA. Scale bar = 1 µm

Synthesis of MnO_x nanoparticles with dimethylformamide and acetonitrile in the presence of butyric acid showed results that more closely resembled MnO_x-BA. The spheres formed are fairly monodisperse and are of comparable sizes to the control hollow spheres (Figure 43).

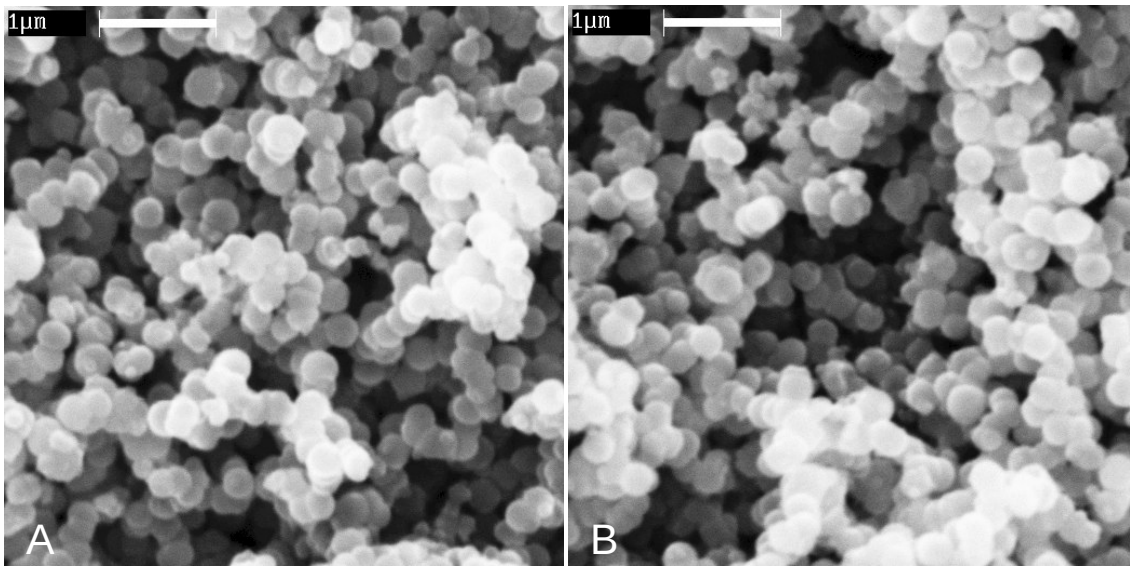

Figure 43. A) 10% Acetonitrile with BA B) 10% DMF with BA. Scale bar = 1 µm

Due to the substantial difference between the effect of DMSO and DMF/ acetonitrile, the reactivity of $KMnO_4$ and DMSO was tested by stirring $KMnO_4$ in 10% DMSO in H_2O. A brown solid was produced from this reaction. The product was not monodisperse, as different parts of the same sample looked very different (Figure 44). The reaction between $KMnO_4$ and DMSO likely affects the reaction between Mn^{2+} and MnO_4^-, resulting in the difference between the materials in Figure 43 and the MnO_x-BA spheres.

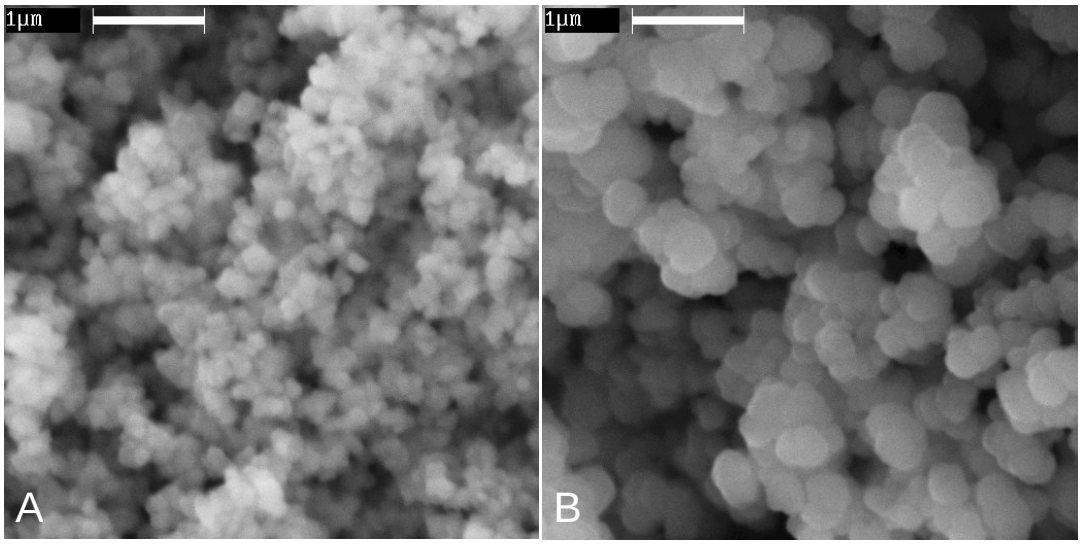

Figure 44. SEM images of DMSO + $KMnO_4$ product: Both taken from same sample. Scale bar = 1 µm

Appendix 4

Control synthesis in 1% milk as a structure-directing agent

The control reaction (MnO_x-C) was carried out in 1% milk as the solvent to test whether the fat particles in milk can act as structure-directing agents for nanoparticle formation. The product consisted of larger particles which slowed the fastest filter frits to a slow drip. The final dried solid was very hard and difficult to grind to a fine powder. The product had nondescript morphology with no spheres present (Figure 45). High-magnification images were unable to be taken.

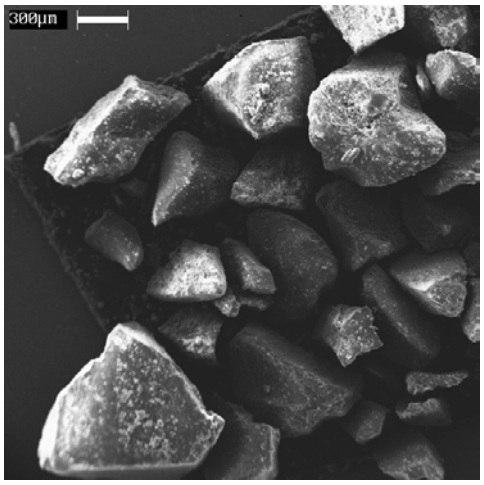

Figure 45. Low-mag SEM image of 1% milk-synthesized material. Scale bar = 300 µm

Control synthesis with sodium dodecylsulfate (SDS) as structure-directing agent

The surfactant, SDS was used in the search for a different structure-directing agent to form hollow spheres. SDS forms micelles in aqueous solution, and it was thought that the micelles could act as a template for the formation of hollow spheres in a similar way to butyric acid. The product had very small particle sizes, and TEM showed that the particles appeared to be uniformly sized (Figure 46). These materials are substantially more difficult to synthesize and work with than the MnO_x-BA materials and give a far lower yield. Therefore, further work on these materials was abandoned.

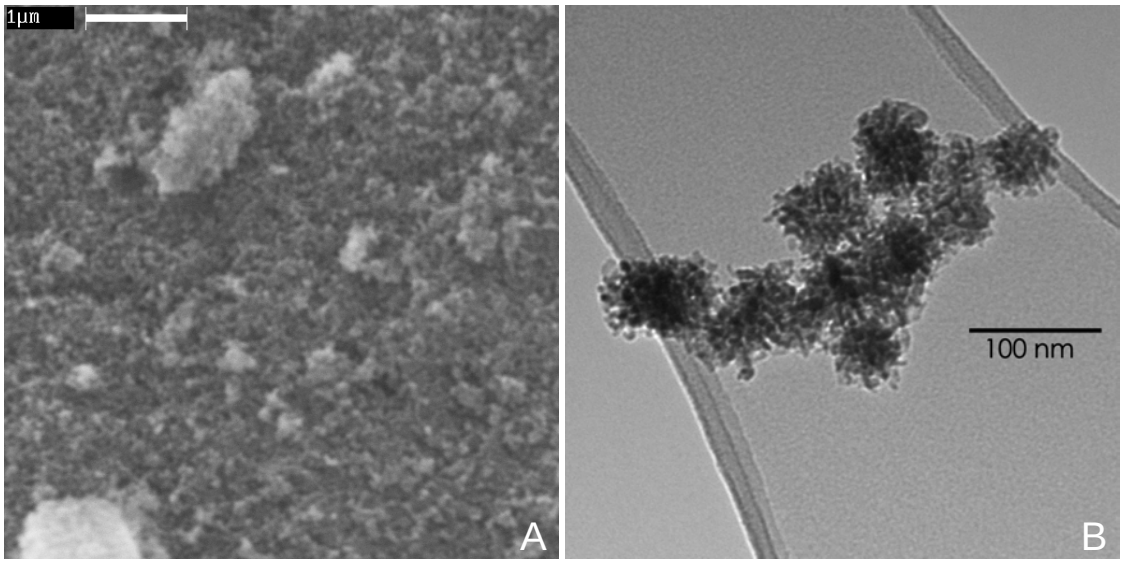

Figure 46. MnO_x synthesized with SDS as structure-directing agent: A) SEM, B) TEM. Scale bar = 1 µm (A), 100 nm (B)

Appendix 5

Effect of Heat on Hollow Sphere Synthesis

The synthesis of hollow nanospheres was done at high and low temperatures in order to see the effect of heat on the size and morphology of the nanoparticles. The spherical monodispersity was lost in both the hot and cold sample. At low temperatures, the particles became larger while losing some of their spherical characteristics. At high temperatures, the particles grew smaller and have a crumpled-tissue-paper morphology comparable to that of the control hollow spheres (Figure 47).

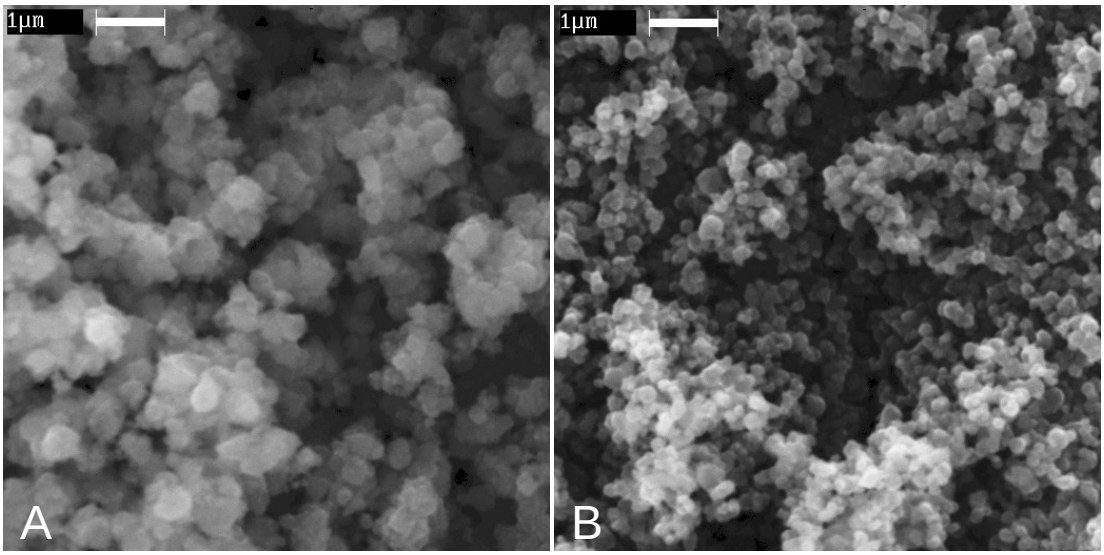

Figure 47. A) MnO_x's synthesized at 4° C, B) MnO_x's synthesized at 60° C. Scale bar = 1 µm

References:

1) Post, J.E*., Proc. Natl. Acad. Sci.* **1999,** *96*, 3447-3454

2) Perry, R.; Adams, J., *Nature* (London), **1978**, *276*, 491

3) Achurra, L.E.; Lacassie, J.P.; Le Roux, J.P.; Marquardt, C.; Belmar, M.; Ruiz-del-solar, J.; Ishman, S.E. *Sedimentary Geology*, **2009**, *217,* 128-139

4) Park, M. S.; Yoon, W. Y. *J. Power Sources.* **2003,** *114, 237-243.*

5) Luo, J. Y.; Xiong, H. M.; Xia, Y. Y. *J. Phys. Chem. C.* **2008,** *112,* 12051-12057

6) Nitta, M. *Appl. Catal.* **1984,** *9,* 151.

7) Cao, J.; Zhu, Y.; Shi, L.; Bao, K.; Liu, S.; Qian Y. *Eur. J. Inorg. Chem.* **2010,** 1172-1176.

8) Stobbe, E.R.; de Boer, B.A.; Geus, J.W. *Catal. Today.* **1999,** *47,* 161-167.

9) Pratt, E.F.; Van de Castle, J.F; *J. Org. Chem.* **1961,** *26,* 2973-2975.

10) Fu, X.; Feng, J.; Wang, H.; Ng, K.M. *Catal. Comm.* **2009,** *10,* 1844-1848

11) Oh, S.H.; Sinkevitch, R.M. *J. Catalysis.* **1993**, *142,* 254-262.

12) Njagi, E.C.; Chen, C.H.; Genuino, H.; Galindo, H.; Huang, H.; Suib, S.L. *Appl. Catal. B*; **2010**, *31*, 103-110

13) Chen, C.H.; Njagi, E.C.; Sun, S.P.; Genuino, H.; Hu, B.; Suib, S. *Chem. Mat.* **2010**. 22, 3313-3315

14) Hoflund, G.B.; Gardner, S.D.; Schryer, D.R.; Upchurch, B.T.; Kielin, E.J. *Langmuir*, **1995**, *11*, 3431-3434

15) Hutchings, G.J.; Mirzaei, A.A.; Joyner, R.W.; Siddiqui, M.R.H.; Taylor, S.H. *Appl. Catal. A.* **1998**, *166*, 143-152

16) Whitesall, W.A.; Frazer, J.C.W. J. Am. Chem. Soc. **1923**, *45*, 2841-2851

17) Li, X.; Hu, B.; Suib, S.; Lei, Y.; Li, B. *J. Power Sources.* **2010**, *195*, 2586-2591

18) Doornkamp, C.; Ponec, V.*J. Mol. Catal.*; **2000**. *162*, 19-32

19) Portehalult, D.; Cassaignon, S.; Baudrin, E.; Jolivet, J. *Chem. Mater.* **2007,** *19,* 5410-5417.

20) Brock, S.L.; Sanabria, M.; Nair, J.; Suib, S.L.; Ressler, T.*J. Phys. Chem. B* **2001,** *105,* 5404-5410

21) Zhang, Q.; Luo, J.; Vileno, E.; Suib, S. L. *Chem. Mater.* **1997,** *9,* 2090-2095.

22) Kai, K.; Yoshida, Y.; Kageyama, H.; Saito, G.; Ishigaki, T.; Furukawa, Y.; Jawamata, J. *J. Am. Chem. Soc.* **2008,** *130,* 15938-15943.

23) Shen, X.; Ding, Y.; Liu, J.; Laubernds, K.; Zerger, R.P.; Polverejan, M.; Son, Y.C.; Aindow, M.; Suib, S.L. *Chem. Mater.* **2004***, 16,* 5327-5335.

24) Ching, S.; Roark, J. L.; Duan, N.; Suib, S. L. *Chem. Mater.* **1997,** *9,* 750-754.

25) Brock, S. L.; Duan, N.; Tiam Z. R.; Giraldo, O.; Zhou, H.; Suib, S. L. *Chem. Mater.* **1998**, *10,* 2619-2628.

26) Portehault, D.; Cassaignon, S.; Baudrin, E.; Jolivet, J. *J. Mat. Chem.* **2009,** *19,* 2407-2416.

27) Portehault, D.; Cassaignon, S.; Nassif, N.; Baudrin, E.; Jolivet, J. *Angew. Chem. Int. Ed.* **2008,** *47,* 6441-6444.

28) Chen, H.; He J. *Chem. Lett.* **2007,** *36,* 174-175.

29) Yuan, J.; Li, W.; Gomez, S.; Suib, S. *J. Am. Chem. Soc.* **2005,** *127,* 14184-14185.

30) Xu, M.; Kong, L.; Zhou, W.; Li, Hulin. *J. Phys. Chem. C.* **2007,** *111*, 19141-19147.

31) Jolivet, J.; Cassaignon, S.; Chanéac, C.; Chiche, D.; Durupthy, O.; Portehault, D. *C. R. Chimie*., **2010,** *13*, 40-51.

32) Portehault, D.; Cassaignon, S.; Baudrin, E.; Jolivet, J. *Chem. Mater.* **2008,** *20,* 6140, 6147.

33) Xu, M.; Kong, L.; Zhou, W.; Li, H. *J. Phys. Chem. C.* **2007,** *111,* 19141-19147.

34) Tang, X.; Liu, Z.; Zhang, C.; Yang, Z.; Wang, Z.; *J. Power Sources*. **2009**, *193, 2,* 939-943

35) Li, B.; Rong, G.; Huang, L.; Feng, C. *Inorg. Chem.* **2006,** *45,* 6404-6410.

36) Yu, P.; Zhang, X.; Chen, Y.; Ma, Y. *Mat. Lett.* **2010,** *64,* 1480-1482.

37) Zeng, H.C. *Curr. Nanosci.* **2007,** *3,* 177-181.

38) Liu B.; Zeng H.C. *Small* **2005,** *5*, 566-577

39) Kriz, David. *Nanostructured Manganese Oxide Catalysts*. **2011**

40) Ching, S.; Kriz, D.; Luthy, K.; Njagi, E.; Suib, S. *ChemComm* **2011**, *47*, 8286-8288

41) Bagai, R.; Christou, G. *Chem. Soc. Rev.* **2009,** *38, 1011-1026.*

42) Schake, A.R.; Tsai, H.; Webb, R., J.; Folting, K.; Christou, G.; Hendrickson, D. N. *Inorg.Chem.* **1994,** *33,* 6020-6028

43) Chen, X.; Shen, Y.; Suib, S. L.; O'Young, C. L. *Chem. Mater.* **2002,** *14,* 940-948

44) Jones, C.; Cole, K.J.; Taylor, S.H.; Crudace M.J.; Hutchings G.J. *J. Mol. Catal.* **2009,** *305*, 121-124

45) Mirzaei, A.A.; Shaterian, H.R.; Habibi, M.; Hutchings, G.J.; Taylor, S.H. *App. Catal.* **2003**, *253*, 499-508

46) Toupin, M.; Brousse, T.; Belange, D. *Chem. Mater.*, **2004**, *16*, 3184

47) Chen, H.; He J.; Zhang C.; He H. *J. Phys. Chem. C,* **2007**, *111*, 18033

48) Cao, J.; Zhu, Y.; Bao, K.: Shi, L.; Liu, S.; Quan, Y. *J. Phys. Chem. C,* **2009**, *113*, 17755

49) Wang, N.; Gao, Y.; Gong, J.; Ma, X.; Zhang, X.: Guo, Y.; Qu, L. *Eur. J. Inorg. Chem.,* **2008,** 3827

50) He, X.; Yang, M.; Ni, P.; Li, Y.; Liu, Z.-H. *Colloids Surf. A,* **2010**, *363*, 64

51) Li, Z.; Ding, Y.; Xiong, Y.; Yang, Q.; Xie, Y. *Chem. Commun.,* **2005**, 918

52) Shen, Y.; Zerger, R.; DeGuzman, R.; Suib, S.; McCurdy, L.; Potter, D.; O'Young, C. *Science* **1993**, *260*, 511-515

53) Yuan, J.; Laubernds, K.; Zhang, Q.; Suib, S. *J. Am. Chem. Soc.* **2003**, *17*, 4966-4967

54) Genuino, H.C.; Meng, Y.; Horvath, D.T.; Seraji, M.S.; Morey, A.M.; Joesten, R.L.; Suib, S.L. *Chem. Cat. Chem.*, **2013**, *5*, 2306-2317

55)Iyer, A. Galindo, H.; Sithambaram, S.; King'ondu, C. Chen, C-H.; Suib, S. *App. Catal. A* **2010**, *375*, 295-302

56) Zhou, H.; Wang, J.Y.; Chen, X.; O'Young, C-L.; Suib, S. *Microp. & Mesop. Mats.* **1998**, *21*, 315-324

57) Wang, J-Y.; Xia, G-G.; Yin, Y-G.; Suib, S.; O'Young, C-L. *J. Catal.* **1998**, *176*, 275-284

58) Zhou, H.; Shen, Y.; Wang, J.; Chen, X.; O'Young, C-L.; Suib, S. *J. Catal.* **1998**, *176*, 321-328

59) Tang, X.; Li, J.; Hao, J. *Cat. Comm.*, **2010**, *11*, 871-875

60) Li, M.; Wang, D-H.; Shi, X-C.; Zhang, Z-T.; Dong, T-X. *Sep. & Pur. Tech.* **2007**, *57*, 147-151

61) Rogers, T.H.; Piggot, C.S.; Bahlke, W.H.; Jennings, J.M. *J. Am. Chem. Soc.*, **1921**, *43*, 1973-1982

62) Men-ill, D.R.; Scalione, C.C. *J. Am. Chem. Soc.*, **1921**, *43*, 1982-2002

63) Jones, H.A.; Taylor, H.S. *J. Phys. Chem.*, **1923**, *27*, 623

64) Stone, F.S. *Adv. Catal.* **1962,** *5,* 1

65) Wollner, A.; Lange, F.; Schemelz, H.; Knozinger, H. *Appl. Catal. A* **1993**, *94*, 181

66) Hutchings, G.; Mirzaei, A.A.; Joyner, R.; Siddiqui, M.; Taylor, S. *Catal. Lett.* **1996**, *42*, 21

67) He, X.; Yang, M.; Ni, P.; Li, Y.: Lio, Z-H. *Coll. & Surf. A* **2010**, *363*, 64-70

68) Qian, K.; Qian, Z.; Hua, Q.; Jiang, Z.; Huang, W. *App. Surf. Sci.* **2013**, *273*, 357-363

69) Shen, B.; Liu, T.; Zhao, N.; Yang, X.; Deng, L. *J. Envir. Sci.* **2010,** *22*, 1447-1454

70) Parry, E.P. *J. Catal.*, **1963**, *2*, 371-379

71) Monnell, J.D.; Li, H.; Alvin, M.; Vidic. R. *PCC,* **2008**

72) Xu, Z. P.; Zeng, Q. H.; Lu, G. Q.; Yu, A. B. *Chem. Eng. Sci.* **2006**, *61*, 1027–1040

73) Martin, C. R.; Kohli, P. *Nat. Rev. Drug Discovery* **2003**, *2*, 29–37

74) Caruso, F. *Chem. Eur. J.* **2000**, *6*, 413–419

75) An, Z.; Zhuo, Y,; Xu, C.; Chen, C. *Chinese J. Catal.* **2014**, *35*, 120-126

76) Richardson, P.L.; Perdigoto, M.; Wang, W.; Lopes, R. *Appl. Cat. B* **2012,** *126*, 200-207